University of Leoben

Impact of Al on structure and mechanical properties of NbN and TaN

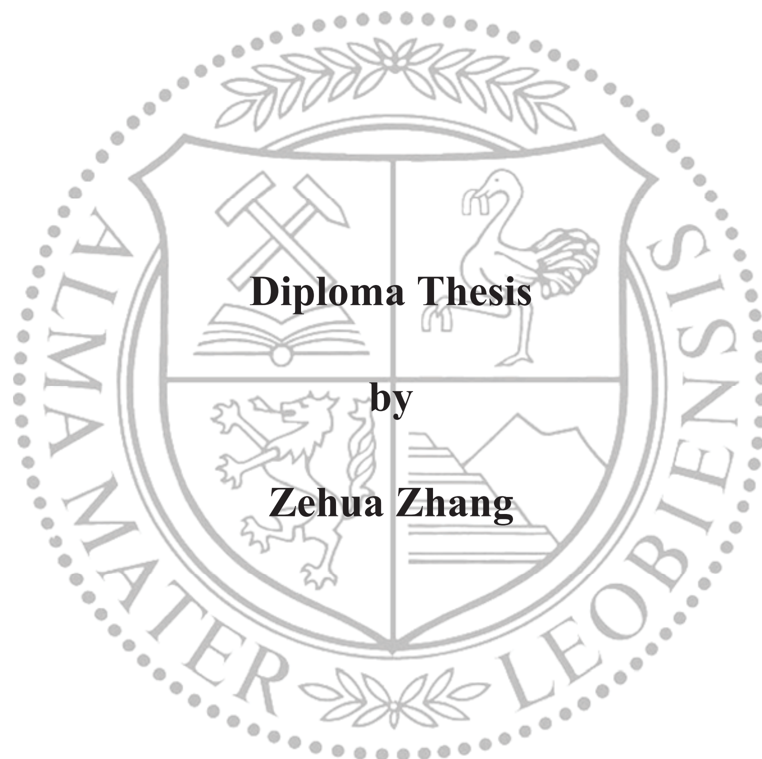

Diploma Thesis

by

Zehua Zhang

Leoben, March 2011

This thesis was supported by the Austrian Science Fund through the project FWF-Start-Project Nr. Y371.

Affidavit:

I declare in lieu of oath, that I worte this thesis and performed the associated research by myself, using only literature cited in this volume.

Leoben, March 2011

Acknowledgements

First and foremost, I would like to express my deeply gratitude to **Assoc.Prof.Dr. Paul Mayrhofer,** a respectable, responsible and resourceful scholar, who has given me the chance writing of this thesis.

I also want to express my deeply gratitude to my supervisor **DI. Richard Rachbauer**, who has provided me with valuable guidance in every stage of the writing of this thesis. Without his enlightening instruction, impressive kindness and patience, I could not have completed my thesis. His keen and vigorous academic observation enlightens me not only in this thesis but also in my future study.

Furthermore, I would like to thank all members of the **Department of Physical Metallurgy and Materials Testing**, who all supported my work.

I owe many thanks to my beloved wife **Lan Wang**, who has shared with me all my difficult times and happy times, and gave me a cute and clever daughter **Olivia Zhang** during the writing of this thesis.

Finally, I wish to express my appreciation to **my family** and **all friends** for their unconditioned love, endless support over those years and for always being there when needed.

Table of contents

Page

Table of contents .... **I**

List of figures .... **IV**

List of tables .... **VI**

1 Introduction **1**

2 Coating deposition **3**

2.1 General 3

2.2 Plasma 5

2.2.1 Fundamentals of plasma 5

2.2.2 Glow discharge 5

2.3 Sputtering 6

2.3.1 DC-sputtering 6

2.3.2 Magnetron sputtering 7

2.4 Thin film growth 8

2.4.1 Nucleation and growth 8

2.4.2 Structure zone models 10

3 Coating systems **13**

3.1 Binary phase diagrams 13

3.1.1 Nb-N 13

3.1.2 Ta-N 14

3.2 Transition zone in pseudobinary transition metal aluminum nitrides 15

4 Experimental **18**

4.1 Film deposition 18

4.1.1 Deposition facility 18

4.1.2 Targets and substrates 19

4.1.3 Deposition pre-cleaning 21

4.2 Characterization 22

4.2.1 X-ray diffraction (XRD) 22

4.2.2 Chemical analyses 23

4.2.3 Coating thickness ……………………………………………………23
4.2.4 Nanoindentation ……………………………………………………24

5 Results and discussion ……………………………………………………26
5.1 NbN_y-thin films ……………………………………………………26
5.1.1 Processing conditions and chemical compositions of NbN_y ……………26
5.1.2 Chemical composition of NbN_y ……………………………………27
5.1.3 Growth rate of NbN_y ……………………………………………28
5.1.4 XRD of NbN_y ……………………………………………………30
5.1.5 Mechanical properties of NbN_y …………………………………31
5.1.6 Comparsion of sturctures at over-stoichiometric compositions of N/Nb ……33
5.1.7 Comparsion of mechanical properties at over-stoichiometric compositions of N/Nb……………………………………………………34
5.2 TaN_y-thin films ……………………………………………………35
5.2.1 Processing conditions and chemical compositions of TaN_y ……………35
5.2.2 Chemical composition of TaN_y ……………………………………36
5.2.3 Growth rate of TaN_y ……………………………………………37
5.2.4 XRD of TaN_y ……………………………………………………38
5.2.5 Mechanical properties of TaN_y …………………………………39
5.2.6 Comparsion of sturctures at over-stoichiometric compositions of N/Ta ……42
5.2.7 Comparsion of mechanical properties at over-stoichiometric compositions of N/Ta……………………………………………………43
5.3 $Nb_{1-x}Al_xN$-thin films ……………………………………………44
5.3.1 Processing conditions and chemical compositions of $Nb_{1-x}Al_xN$ ………44
5.3.2 Colours of $Nb_{1-x}Al_xN$ …………………………………………45
5.3.3 Phases of $Nb_{1-x}Al_xN$ …………………………………………46
5.3.4 Lattice parameters of $Nb_{1-x}Al_xN$ ………………………………47
5.3.5 Growth rate of $Nb_{1-x}Al_xN$ ……………………………………49
5.3.6 Mechanical properties of $Nb_{1-x}Al_xN$ …………………………50
5.4 $Ta_{1-x}Al_xN$-thin films ……………………………………………51
5.4.1 Processing conditions and chemical compositions of $Ta_{1-x}Al_xN$ ………51
5.4.2 Colours of $Ta_{1-x}Al_xN$ …………………………………………52
5.4.3 Phases of $Ta_{1-x}Al_xN$ …………………………………………53
5.4.4 Lattice parameters of $Ta_{1-x}Al_xN$ ………………………………54

5.4.5 Growth rate of $Ta_{1-x}Al_xN$ ……………………………………..………...………....55
5.4.6 Mechanical properties of $Ta_{1-x}Al_xN$ …………………………………….…..…..56

6 Summary and conclusion...**58**

References……………………………………………………………………………..**60**

List of figures

Page

Fig. 2.1: Basic variations of PVD……………………………...…..…………………………….5
Fig. 2.2: Characteristic voltage and current of a DC glow discharge………..………………..6
Fig. 2.3: Schematic interaction processes during DC-sputtering: (a) Ionisation of gas atoms by impacting electron, (b) electron emission from the cathode, (c) electron emission from the anode, (d) sputtering of neutrals from the cathode, (e) charge transition process……..…………………………………………………………..…………7
Fig. 2.4: (a) Schematic of balanced magnetron and (b) unbalanced magnetron (UBM)……..8
Fig. 2.5: A schematic drawing of nucleation and growth processes…….……………………9
Fig. 2.6: Nucleation modes……………………………………………….…………………10
Fig. 2.7: Structure zone model from Movchan and Demchishin…………....………..……...10
Fig. 2.8: (a) Structure zone models after Thornton and, (b) Messier…...……………………11
Fig. 2.9: Schematic representation of the physical processes underlying the Thornton structure zone model (SZM) consisting of the zones 1, T, 2, 3…………………...……….12
Fig. 3.1: Binary phase diagram of Nb-N…………………………………….………………13
Fig. 3.2: Binary phase diagram of Ta-N……………..…………………………….………..14
Fig. 3.3: Structural changes with increasing Al-content...…………………………….….….16
Fig. 3.4: a) Hardness and lattice parameter of $Ti_{1-x}Al_xN$ coatings as a function of Al-content. b) Hardness and Young’s modulus of $Ti_{1-x}Al_xN$ coatings as a function of Al-content. ……………………………………………………………………………………..16
Fig. 3.5: Hardness and Young’s modulus of $Nb_{1-x}Al_xN$ coatings as a function of Al-content17
Fig. 4.1: Schematic drawing and photo of the lab-scale UBM-sputter plant……….……..18
Fig. 4.2: Schematic drawing of the Al-platelet position on the Nb or Ta targets for the deposition of $Ta_{1-x}Al_xN$ and $Nb_{1-x}Al_xN$, respectively…………...…………………...…..20
Fig. 4.3: Schematic θ-2θ scan mode by XRD………..……………………………...……22
Fig. 4.4: Ball-Crater-Test in 2D drawing…….……………………………………………24
Fig. 4.5: Schematic of a load-displacement curve…………..…...…………………………...25
Fig. 5.1: N/Nb atomic ratio for NbN_y with increasing P_{N2}/ P_T during deposition…………...28
Fig. 5.2: (a) Growth rate and (b) target voltage for NbN_y with increasing P_{N2}/P_T…………..28
Fig. 5.3: XRD-patterns of as-deposited NbN_y-films with increasing P_{N2}/ P_T during deposition (a) at varying total pressure and, (b) at constant P_T = 0.30 Pa……….………....…30

Fig. 5.4: Hardness and Young's modulus of NbN_y as a function of P_{N2}/P_T during deposition ……………………………………………………………………………………..31
Fig. 5.5: XRD-patterns of as-deposited NbN_y-films with increasing N content (a) in the range from N/Nb = 1.00 to 1.16 and, (b) in the range from N/Nb = 1.20 to 1.36..33
Fig. 5.6: Hardness and Young's modulus of as-deposited NbN_y-films with increasing N content (a) in the range from N/Nb = 1.00 to 1.16 and, (b) in the range from N/Nb = 1.20 to 1.36……………………………………………………………...34
Fig. 5.7: N/Ta atomic ratio for TaN_y with increasing P_{N2}/P_T during deposition..……........36
Fig. 5.8: (a) Growth rate and (b) target voltage for TaN_y with increasing P_{N2}/P_T…………37
Fig. 5.9: XRD patterns for TaN_y-films with increasing P_{N2}/P_T during deposition (a) at varying total pressure and, (b) at constant P_T = 0.3 Pa……………………..….38
Fig. 5.10: Hardness and Young's modulus of TaN_y as a function of P_{N2}/P_T during deposition ……………………………………………………………………………...39
Fig. 5.11: Different cracks on the surface of as-deposited TaN_y-films with increasing P_{N2}/P_T (a) P_{N2}/P_T=60%, N/Ta=1.35 (b) P_{N2}/P_T =70%, N/Ta=1.25 (c) P_{N2}/P_T =80%, N/Ta=1.35 (d) P_{N2}/P_T =90%, N/Ta=1.61 (d) P_{N2}=100%, N/Ta=1.46....................41
Fig. 5.12: XRD-patterns of as-deposited TaN_y-films with increasing N-content (a) in the range from N/Ta = 1.04 to 1.13 and, (b) in the range from N/Ta = 1.24 to 1.61…42
Fig. 5.13: Hardness and Young's modulus of as-deposited TaN_y-films with increasing N content (a) in the range from N/Ta = 1.04 to 1.13 and, (b) in the range from N/Ta = 1.24 to 1.61……………………………………………………………………….43
Fig. 5.14: Different colours with increasing Al-content of the $Nb_{1-x}Al_xN$ coatings………...45
Fig. 5.15: XRD patterns of $Nb_{1-x}Al_xN$ coatings……………………………………………...46
Fig. 5.16: (a) Lattice parameter of $Nb_{1-x}Al_xN$ as a function of Al-content. (b) Schematic representation of the solid-solution in a fcc-$Nb_{1-x}Al_xN$ crystal............................47
Fig. 5.17: Growth rate of $Nb_{1-x}Al_xN$ as a function of Al-content…………………………...49
Fig. 5.18: Hardness and Young's modulus of as-deposited $Nb_{1-x}Al_xN$-coatings………..….50
Fig. 5.19: Different colours with increasing Al-content of the $Ta_{1-x}Al_xN$ coatings…..…......52
Fig. 5.20: XRD patterns of $Ta_{1-x}Al_xN$ coatings……………………………………………..53
Fig. 5.21: (a) Lattice parameter of $Ta_{1-x}Al_xN$ as a function of Al-content. (b) Schematic representation of the solid-solution in a fcc-$Ta_{1-x}Al_xN$ crystal……………..……54
Fig. 5.22: Growth rate of $Ta_{1-x}Al_xN$ as a function of Al-content…………………..……...55
Fig. 5.23: Hardness and Young's modulus of as-deposited $Ta_{1-x}Al_xN$-coatings……….…....56

List of tables

Page

Table 3.1: Crystal structures and lattice parameters of Nb-N……………………………….14

Table 3.2: Crystal structures and lattice parameters of Ta-N………………………………...15

Table 4.1: Target materials……………………………………..……………………...19

Table 4.2: Substrate materials and main investigation………………………………………20

Table 4.3: Parameters used for X-ray investigations……………………………………..…..23

Table 5.1: Deposition parameters and chemical composition of NbN_y films deposited at varying total pressure……………………………………………………………26

Table 5.2: Deposition parameters and chemical composition of NbN_y films deposited at constant P_T = 0.3 Pa…..…………………………………………………………..27

Table 5.3: Deposition parameters and chemical composition of TaN_y films deposited at varying total pressure……………………………………………………………35

Table 5.4: Deposition parameters and chemical composition of TaN_y films deposited at constant P_T = 0.3 Pa...……………………………………………………………..…36

Table 5.5: Chemical composition of the deposited films and used numbers of Al platelets on the Nb-target during deposition with P_T = 0.30 Pa, P_{N2}/ P_T = 42%, T_s = 500 ^oC, and V_b = -50 V……………………..……………………………………...……….…44

Table 5.6: Chemical composition of the deposited films and used numbers of Al platelets on the Ta-target during deposition with P_T = 0.45 Pa, P_{N2}/ P_T = 26%, T_s = 500 ^oC, and V_b = -50 V……………..…………………………………………………….…....51

1. Introduction

In industrialized countries, friction consumes ~30% of all energy generated. Further on about 1-2% of the gross national product are lost due to combined friction and wear. Therefore surface modification techniques are widely researched in order to improve the wear resistance of materials. In many cases coatings are applied to improve the surface properties of the substrate, such as appearance, oxidation resistance, adhesion, wettability, corrosion or wear resistance [1].

Nowadays, hard coatings such as transition metal nitrides, carbides or borides are widely used for wear-resistance in machining, casting or hot-forming applications [2]. For instance, TiN films exhibit high hardness and good wear resistance. However, TiN oxidises above 550°C to form rutile-structure TiO_2, whose porous morphology enables for rapid growth of the oxide scale. Therefore, ternary compounds of (Ti,X)N are researched on to improve the oxidation resistance of TiN films. $Ti_{1-x}Al_xN$ coatings have become the most widely used coating system for dry machining due to their high melting point, oxidation resistance and excellent mechanical properties [3].

Basically, the coating's structure and properties of $Ti_{1-x}Al_xN$ depend on their deposition technique, parameter and chemical composition. The Al content of $Ti_{1-x}Al_xN$ coatings has a significant effect on their structure and mechanical properties.

As soon as the Al content exceeds the cubic solid solubility limit, a mixed structure of cubic- (B1, NaCl-prototype) and hexagonal (B4, ZnS-wurtzite-prototype) is formed, typically in the range of $0.64<x<0.74$ [2], before a single phase wurtzite structure is formed. This structure change typically goes along with a decrease in hardness. Ternary nitrides e.g., Ti-Al-N and Cr-Al-N have been extensively studied in the past. But also other transition metals form stable binary nitrides, such as NbN_y, TaN_y, ZrN_y and HfN_y. Among these nitride coatings, NbN_y coatings are of increasing interest because of their high hardness, wear resistance and superconducting properties [4]. TaN_y coatings have many advantageous properties, such as a high melting point, high hardness and excellent corrosion resistance [5]. TaN is presently

used in electronics industry, and finds its application for thin film resistors and diffusion barriers [4-5].

In this work, first of all, a series of NbN_y and TaN_y coatings are deposited on Si and austenitic stainless steel substrates by a reactive unbalanced magnetron sputtering technique. The films are then characterized by X-ray diffraction (XRD), scanning electron microscopy (SEM), and nanoindentation. These studies were necessary to find the deposition parameters to grow single-phase face centered cubic (fcc) NbN and TaN.

Furthermore, the fcc-NbN and fcc-TaN phases are alloyed with Al to form ternary $Nb_{1-x}Al_xN$ and $Ta_{1-x}Al_xN$ coatings. The resulting structures and mechanical properties are discussed as a function of the Al-content.

2 Coating deposition

2.1 General

Surface engineering (by creating or modifying surfaces) enables for improvement of wear and corrosion performance, fatigue resistance or biocompatibility of materials. The wide range of industrial use thus implements the need for various surface engineering techniques, which can be devided into surface modification and coating depositing which itself can be classified into [6]:

- By surface modification outer regions of a material are modified. The thickness can be between 0.1 µm and 10 mm. Different treatments are possible [6-7]:

  * Mechanical treatments: e.g., shot-peening.

  * Thermal treatments: e.g., flame hardening, laser hardening.

  * Thermochemical treatments: e.g., carburising, nitriding.

- Coating deposition is used to cover a substrate with another material. The thickness can range between 0.001 µm up to 10 mm. Different methods are used [6-7]:

  * Mechanical: e.g., cladding, bonding.

  * Thermal: e.g., welding (laser, plasma….).

  * Electro-chemical: e.g., electro galvanizing.

  * Thermal spraying: e.g., flame, plasma, detonation gun.

  * Chemical vapour deposition (CVD).

  * Physical vapour deposition (PVD).

Both methods PVD and CVD use a vapourised material to deposit the required coating on the substrates. CVD processes are typically carried out at a temperature above 800-900 ºC, whereby the process has only found widespread usage on materials which can withstand such a temperature without softening or appreciable distortion. Therefore, this technique is limited

to thermally stable materials. In contrast, PVD uses typically low deposition temperatures of $\leq 500\ ^{o}C$. Therefore, various substrates, such as alloys, metals, ceramics, as well as glass and even polymers can be used. A major difference between CVD and PVD is, that for PVD the major vapour phase is generated by a physical process like evaporation or sputtering, whereas in CVD all vapour compounds are generated by a chemical process. The formation of a compound coating with PVD requires also chemical reactions at the substrate surface [6].

In general a PVD process follows a sequence of steps: (1) The target material is converted into a vapour by physical means in a vacuum chamber, (2) the vapour is transferred to the substrate, (3) then the vapour is deposited on a substrate. By the method how the target material is converted into a vapour the PVD processes can be classified in three general categories [6]:

- Evaporation: (e.g., resistive, inductive, electron gun, arc)

  During thermal evaporation (Fig. 2.1), the target material is heated in a sufficiently high vacuum (10^{-3} to 10^{-6} Pa), until it evaporates. The distance between target and substrate has to be short enough to ensure that the metallic vapour reaches the substrate, where it condensates [8].

- Sputtering: (e.g., diode, magnetron, ion beam, triode)

  In the sputtering process (Fig. 2.1), a plasma is ignited between the target (cathode) and the substrate (anode). Thereby the target material is subjected to a constant bombardment by ionized working gas particles with high kinetic energy. The surface atoms of the target are directly ejected from the solid phase into the vapour phase [8]. This method is used in this thesis. Therefore, this process will be discussed in more detail in chapter 2.3.

- Ion plating:

  Ion plating (Fig. 2.1), can be regarded as a hybrid process between sputtering and evaporation. The coating material will be vaporised and then the atoms are ionised by a glow-discharge produced by biasing the substrate to a high negative potential and employing a working gas. Finally, the coating material is deposited onto the substrate.

The benefit of this process is that the deposition rates are high, but the coatings usually have unevenly distributed coating thicknesses. The substrate temperature can be relatively low, sometimes below 300 ^oC [8].

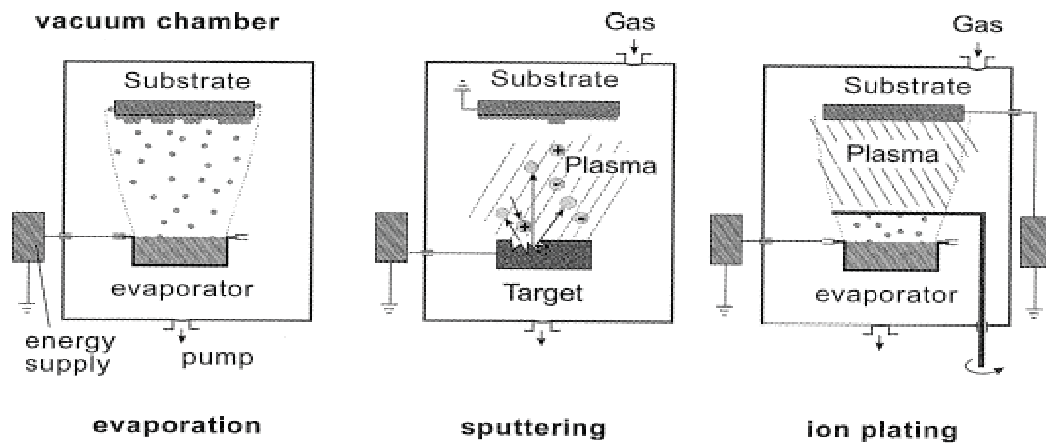

Fig. 2.1: Basic variations of PVD [8].

2.2 Plasma

A plasma is also called “quasi-neutral gas”, due to the fact that plasma species consist of a collection of electrons, ions, and neutral atomic and molecular species exhibiting collective behavior und are in summary neutral [9]. A plasma can be generated in a low pressure process by applying a sufficiently high voltage between two electrical poles [10].

2.2.1 Fundamentals of plasma

The negative charge carriers are primarily electrons and the positive charge carriers are ions from the working gas (e.g., Ar) and/or reactive gas (e.g., N_2, O_2).

2.2.2 Glow discharge

A DC glow discharge is generated by applying a potential between two electrodes in a gas, as presented in Fig. 2.2. At first, a small voltage includes only a small number of charge carriers in the system. By increasing the voltage, the current density increases rapidly until a Townsend value V_b, where the current density increases without further increase of the potential, due to the limitation of the output impedance of the power supply. This region is

called the Townsend discharge. As soon as enough charge carriers are produced during the ionization, a self-sustaining plasma region is reached. The region between ~ 10^{-6} to 10^{-2} (A/cm^2) is characterized by a plasma requiring less voltage than in the Townsend region to sustain the plasma discharge. The ion bombardment can be spread over the entire cathode surface with increasing power. A further increase in power leads to a discharge also near the edges and preferably at surface irregularities. At the same time this results in a higher voltage and cathode current-density levels. This behavior is called abnormal discharge. This discharge is the operational domain for sputtering. The further increase of current results in the formation of an arc discharge, which exhibits very high currents and ionization rates [9,11].

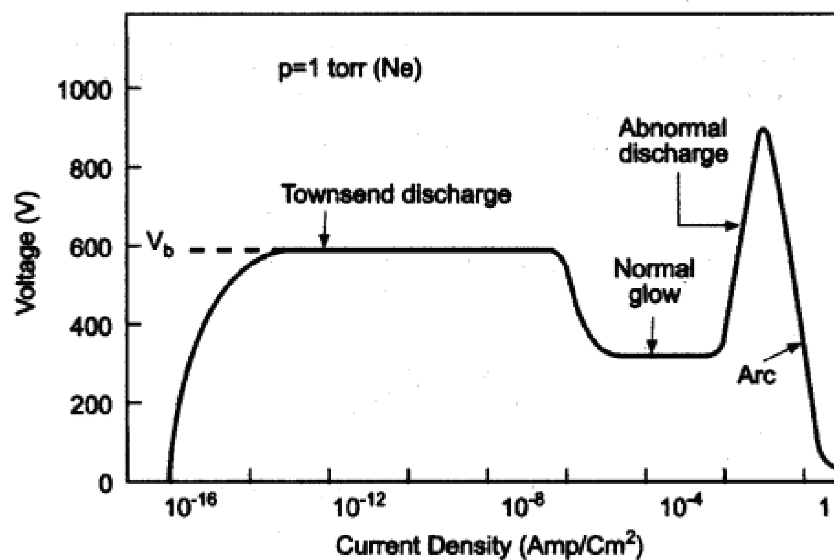

Fig. 2.2: Characteristic voltage and current of a DC glow discharge [11].

2.3 Sputtering

2.3.1 DC Sputtering

Sputtering takes place in a vacuum chamber where a cathode opposes an anode and an electrical field is applied. The negative potential lies at the cathode and the positive at the anode, as presented in Fig. 2.3.

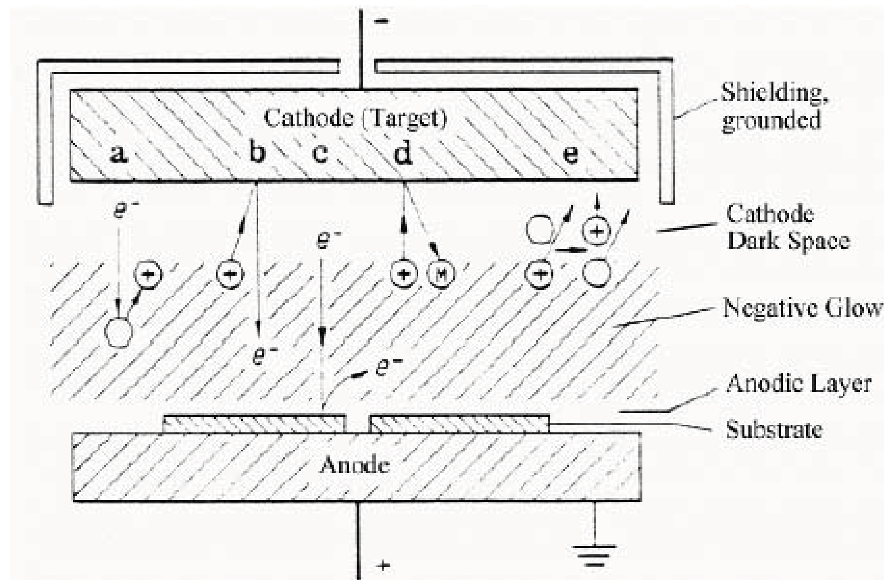

Fig. 2.3: Schematic interaction processes during DC-sputtering: (a) Ionisation of gas atoms by impacting electron, (b) electron emission from the cathode, (c) electron emission from the anode, (d) sputtering of neutrals from the cathode, (e) charge transition process [12].

The total pressure during sputtering plays an important role for the sputter yield. If the pressure is too high, the ejected atoms from the target undergo many collisions with gas atoms. Consequently, these loose energy and are not efficiently transferred to the target. On the other hand, if the pressure is too low, the glow discharge can not be sustained. Therefore, the sputter rate decreases, thus decreasing the ionisation of gas atoms [9].

Applying a (negative) potential on the anode (substrate) is called bias voltage, which is usually in the range of -50 V to -300 V. Due to the applied voltage, some ions from the working gas are attracted to the substrate. Consequently, the flux and energy of ions is influenced by this bias, which can significantly change the structure and thereby the mechanical properties of the coatings.

2.3.2 Magnetron sputtering

During magnetron sputtering, a magnetic field is applied on the target, as presented in Fig. 2.4. The magnetic field concentrates and intensifies the plasma in the space immediately above the

target, as a result of trapping of electrons near the target surface. Therefore, the ion bombardment and sputtering rates increase with the application of a magnetron [13].

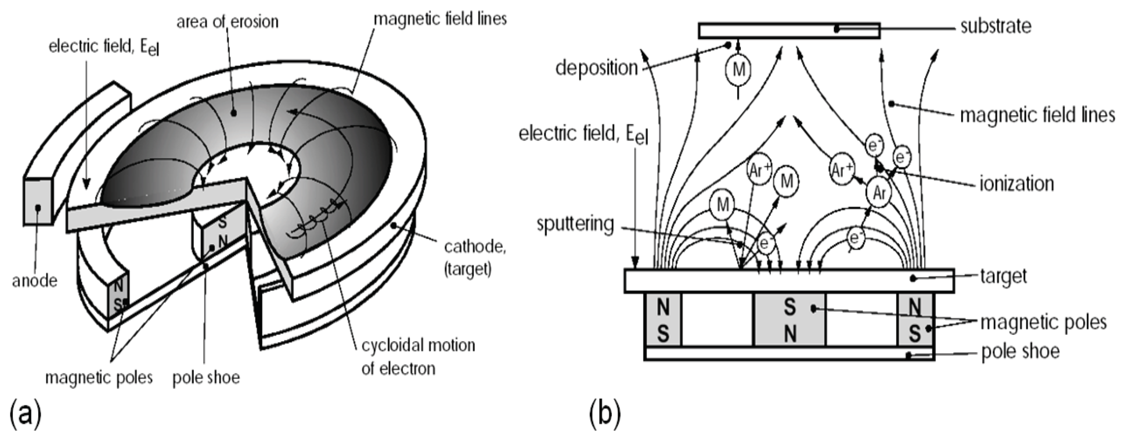

Fig. 2.4: (a) Schematic of balanced magnetron and (b) unbalanced magnetron (UBM) [14].

The magnetron devices can be divided into two types: conventional balanced magnetron (CBM) in Fig. 2.4 (a) and the unbalanced magnetron (UBM) in Fig. 2.4 (b). In CBM all magnetic field lines loop ideally between the outer and the inner magnet of the magnetron configuration, which means that they are balanced against each other. Therefore, the discharge is forced close to the target. In UBM configuration, which is used in this thesis, the magnetic field lines are opened towards the substrate. Thus, the plasma is also stretching towards the substrate, and hence bombardment of the substrate with energetic particles is possible. By an additional bombardment and transfer of kinetic energy to the film forming species their diffusivity increases. This strongly influences e.g., crystal structure, stress development and mechanical properties [15].

2.4 Thin film growth

2.4.1 Nucleation and growth

The structure of the deposited thin film is often determined by nucleation processes (Fig. 2.5). The atoms impinge on the surface with a certain arrival rate and are either directly reflected or adsorbed. Atoms which dwell on the surface are able to diffuse or exchange their energy with

other atoms or the lattice or they desorb again. Due to the different chemical nature of the coating material and the substrate, deposition atoms can not immediately condense on the surface. Several "single" atoms form a cluster which is able to condense on the substrate. This process is called nucleation. Single adsorbed atoms diffuse on the surface and attach to existing clusters. This process is called growth [11,14].

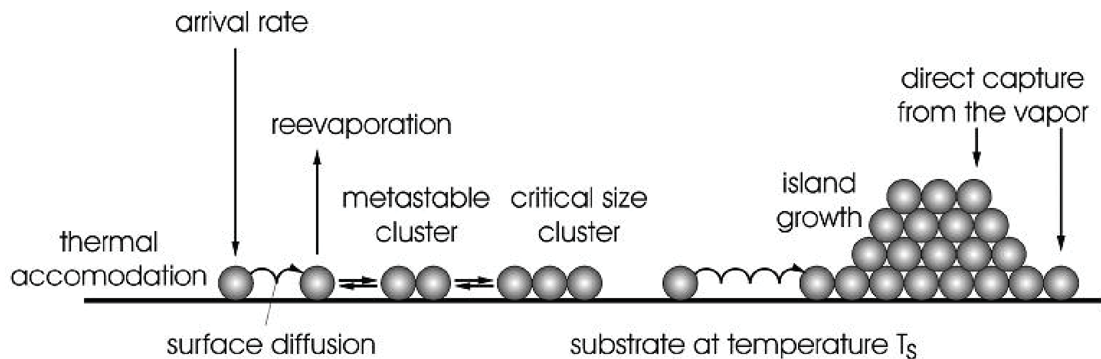

Fig. 2.5: A schematic drawing of nucleation and growth processes [14,16].

For the nucleation of crystals three models are reported, which can occur depending on binding energies between atom-atom and atom-substrate, as presented in Fig. 2.6. Within the layer mode or Frank-van der Merwe mode (Fig. 2.6a), the growing films form a complete layer as the binding energy of deposited atoms to each other is weaker than to the substrate. The island mode or Volmer-Weber mode (Fig. 2.6b) exhibits the opposite characteristic, where the binding energy of deposited atoms to each other is stronger than to the substrate. Thus, small clusters are formed on the substrate surface and form islands. The layer plus island mode or Stranski-Krastanov mode (Fig. 2.6c), is an intermediate case. At first there is a formation of a monolayer followed by an island growth onto it [9, 11,17].

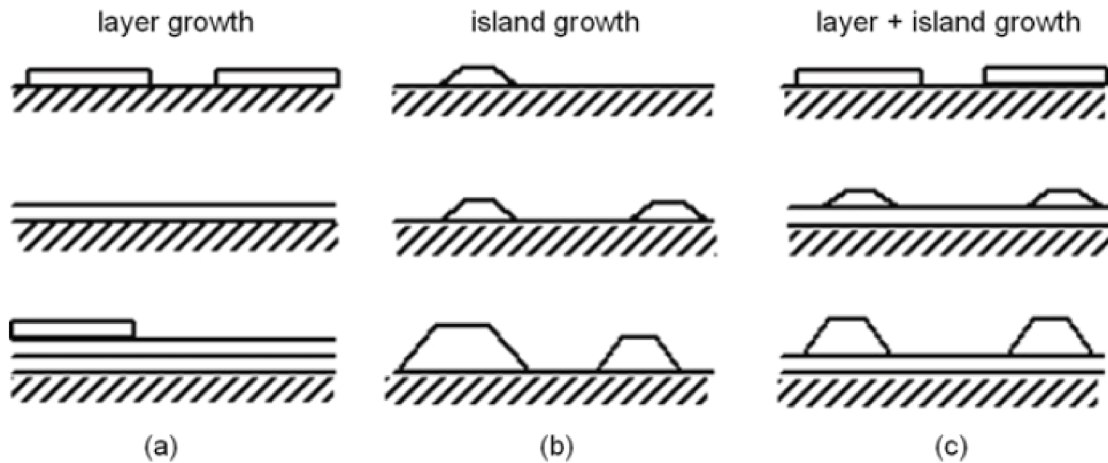

Fig. 2.6: Nucleation modes [17].

2.4.2 Structure zone models

The first structure zone model for thin films was established by Movchan and Demchishin. It describes the impact of condensation, surface diffusion, bulk diffusion, and the recrystallization [11]. This model proposes three structure zones as a function of substrate temperature (T_s) with respect to the melting temperature, as shown in Fig. 2.7.

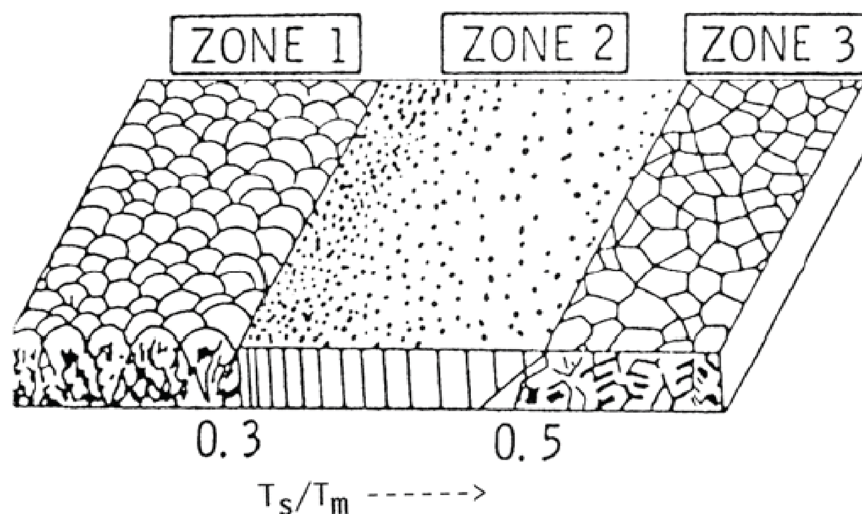

Fig. 2.7: Structure zone model from Movchan and Demchishin [11].

Zone 1 ($T_s/T_m<0.3$) exhibits a "cauliflower-type" structure. Thereby columnar crystals grow with rounded tips. Due to the shadowing effect and limited surface diffusion, the layer is separated by voided boundaries, thus the structure is porous and exhibits a high dislocation density.

Zone 2 ($0.3 \leq T_s/T_m \leq 0.5$) is characterised by a dense columnar structure, due to the higher adatom mobility during growth.

Zone 3 ($0.5 < T_s/T_m$) exhibits a dense structure, consisting of equiaxed crystals. Due to the high temperature, which already enables for bulk diffusion, a coarse-grained morphology can occur in this region [9,11,18].

The Movchan-Demchishin model was modified by Thornton and Messier. They took care of the total gas pressure and the energy of the incident ions (Fig. 2.8). They introduced an additional transition zone T between zone 1 and 2. This zone T is built of a dense array of fibrous grains without pores. As suggested by Thornton (Fig. 2.8a), the development of a zone 1 and T structure requires a higher T_s/T_m when the gas pressure increases. Higher gas pressure leads to more collisions and the particle energy decreases. Thus, the ability for surface diffusion through the adsorbed particles having lower energy is reduced and hence the porosity rises with increasing pressure. Consequently the individual zones are shifted to higher temperatures with higher gas pressure [19,20]. As shown by Messier (Fig. 2.8b), especially the transition between zone 1 and zone T can be shifted towards lower temperatures if a bias potential is applied. The thereby increased ion bombardment of the growing film results in a higher mobility of the film forming species. Thereby the film forming species are more redistributed, the surface roughness decreases, and voids or pores can be filled [11,21].

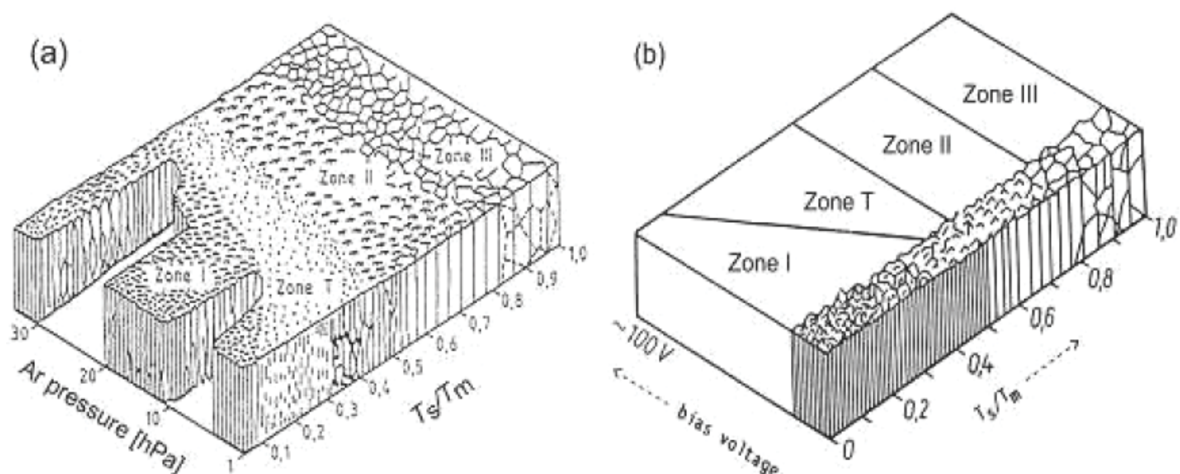

Fig. 2.8: (a) Structure zone models after Thornton [11,19] and, (b) Messier [11,21].

A further investigation on the morphological influence of impurities was undertaken by Barna and Adamik, as shown in Fig. 2.9. Figure 2.9a shows the typical microstructure of a pure coating with respect only to the homologous temperature as already described above. With increasing impurity content (Fig. 2.9b-d) a change of the zone transition temperatures as well as a grain refinement can be observed. At high impurities this leads to diminishing of zone 2 and zone T [22].

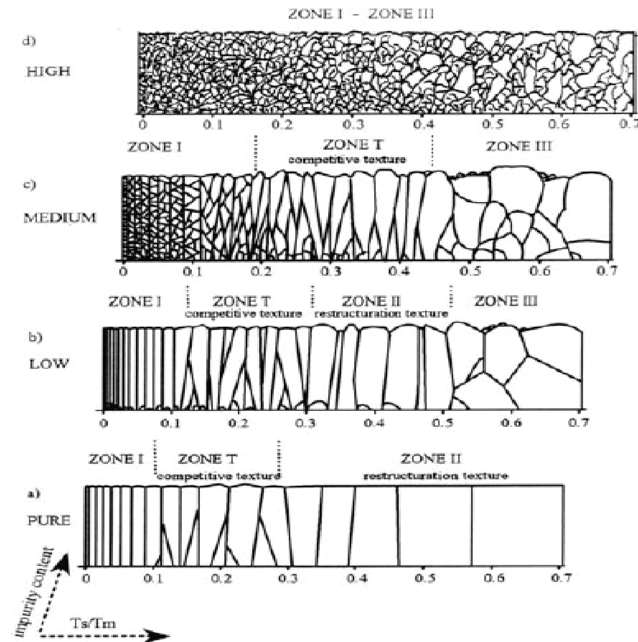

Fig. 2.9: Schematic representation of the physical processes underlying the Thornton structure zone model (SZM) consisting of the zones 1, T, 2, 3 [22].

3 Coating systems

3.1 Binary phase diagrams

Many research activities were done on the superconducting properties of NbN and TaN in the past, but only little information is available on the mechanical properties of these binary nitrides [4,5]. Usually the binary phase diagrams of Nb-N or Ta-N contain 4 phases: (1) a solid solution phase α-M(N) (body centered cubic, bcc), (2) a M_2N (hexagonal) phase, (3) a MN (hexagonal or face centered cubic, fcc) phase and (4) the N-rich phases [24]. One more phase exists in the diagram of Nb-N as compared to Ta-N, which is the ordered γ-Nb_4N_3 phase.

3.1.1 Nb-N

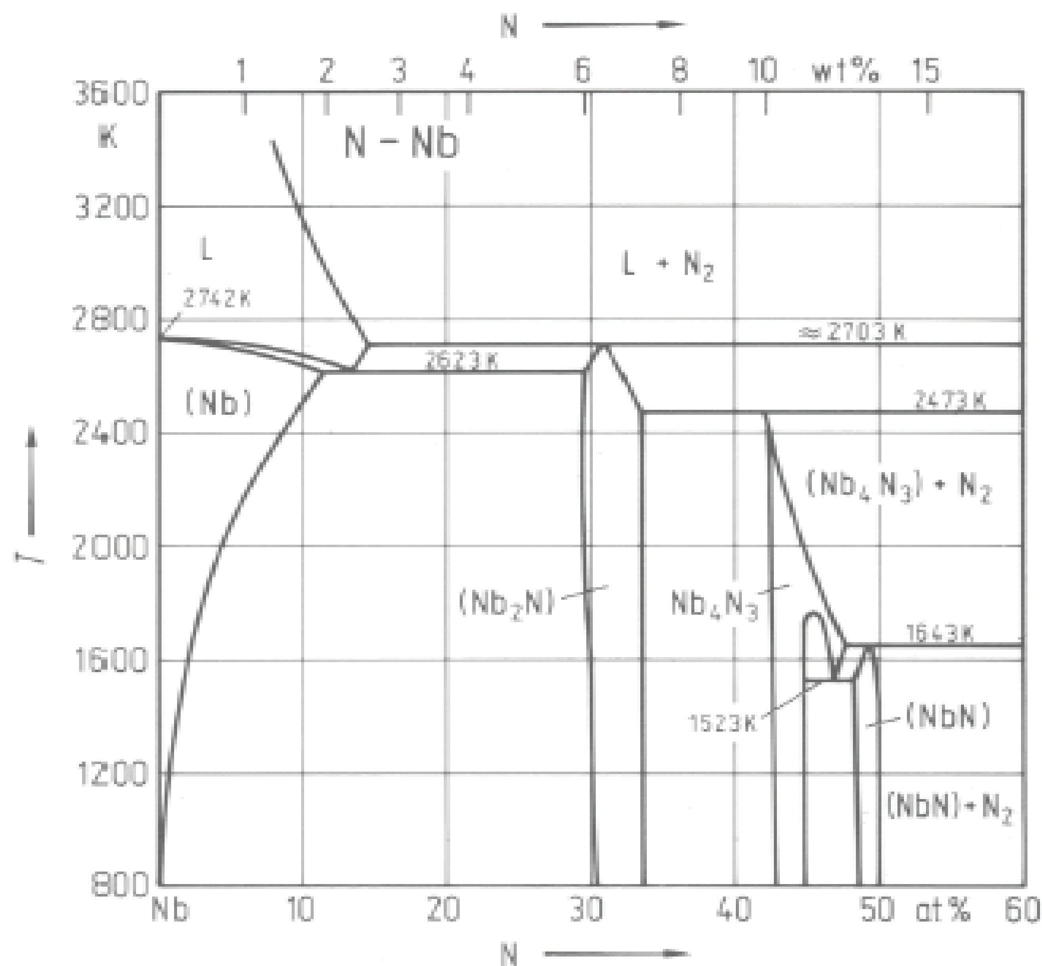

Fig. 3.1: Binary phase diagram of Nb-N [25].

The binary phase diagram of Nb-N is shown as a function of the N mole fraction in Fig. 3.1. The corresponding phases are summarised in Table 3.1, as obtained from the Joint Committee on Powder Diffraction Standards (JCPDS) database [55].

Table 3.1: Crystal structures and lattice parameters of Nb-N.

Phase	Structure	Type	a[nm]	c[nm]	JCPDS-No.card
Nb_2N (β)	hex.	NV_2	0.3058	0.4961	01-089-5129
Nb_4N_3 (γ)	tetr.	N_3Nb_4	0.4382	0.8632	01-089-5131
$Nb_{0.95}N$ (δ’)	hex.	Anti-NiAs	0.2968	0.5535	01-089-4756
NbN (δ)(B1)	fcc	NaCl	0.4394	-	01-071-0162
NbN(ε)	hex.	Anti-NiAs	0.2952	1.1250	01-074-5125
Nb_5N_6	hex.	N_6Nb_5	0.5193	1.0380	01-074-0607

3.1.2 Ta-N

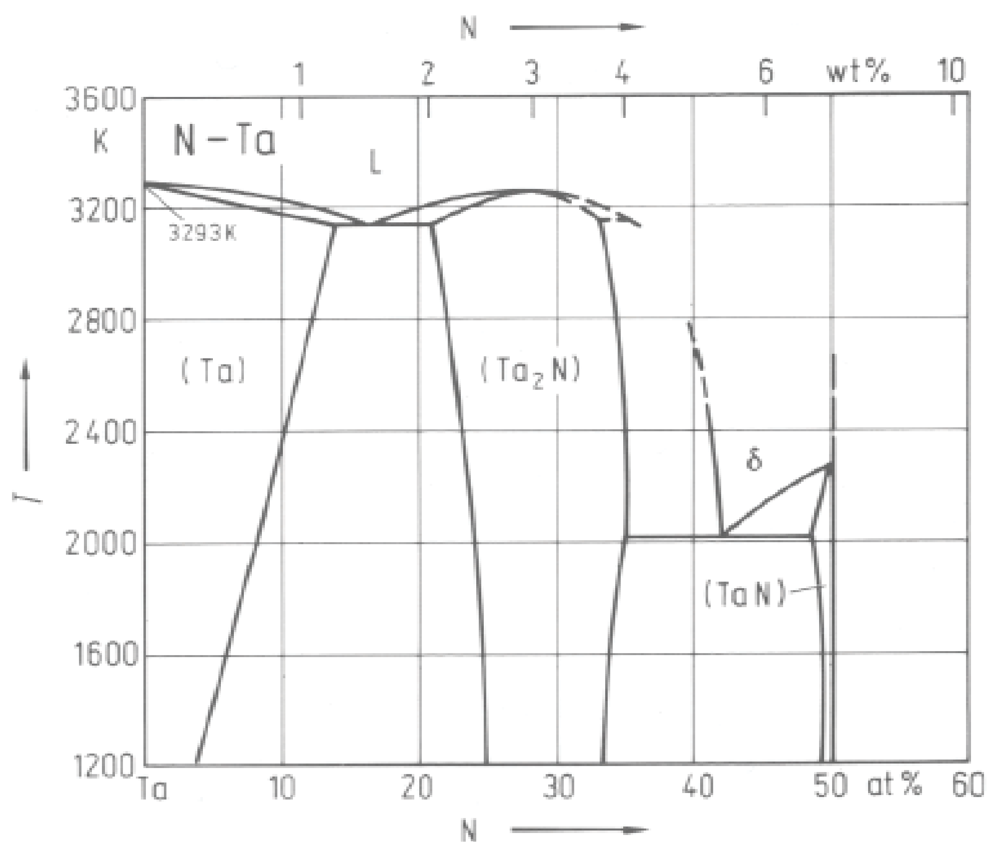

Fig. 3.2 : Binary phase diagram of Ta-N [26].

Figure 3.2 presents the binary phase diagram of Ta-N as a function of the N mole fraction. Table 3.2 shows the corresponding phases from the Joint Committee on Powder Diffraction Standards (JCPDS) database [56].

Table 3.2: Crystal structures and lattice parameters of Ta-N.

Phase	Structure	Type	a[nm]	c[nm]	JCPDS-No.card
Ta_2N (β)	hex.	NiAs	0.3048	0.4918	01-089-4764
TaN(δ)(B1)	fcc	NaCl	0.4420	-	03-065-9404
TaN (ε)	hex.	Anti-NiAs	0.5196	0.2911	01-071-0253
$TaN_{1.13}$	fcc	NaCl	0.4361	-	00-049-1284
Ta_5N_6	hex.	Nb_5N_6	0.5176	1.0353	01-075-0628

3.2 Transition zone in pseudobinary transition metal aluminum nitrides

In various reports [27], it has been shown that the structure change in pseudobinary Ti-Al-N films from cubic structure to wurtzite is affected by the amount of Al dissolved in the lattice, as seen in Fig. 3.3. The AlN content for the B1 (NaCl, fcc) to B4 (wurtzite, hcp) phase change in pesudobinary Ti-Al-N systems corresponds to the maximum solubility of AlN into the transition metal nitride with B1 structure. This transition zone can be found in the range between Al mole fractions of ~0.65 to 0.75, where the coatings often exhibite a mixed cubic and wurtzite structure. As a result of substitution of the Ti atoms with Al, the TiN lattice parameter decreases from 4.255 to 4.216 Å for $Ti_{0.35}Al_{0.65}N$ due to the smaller size of Al atoms as compared to Ti, as seen in Fig. 3.4a [27-29].

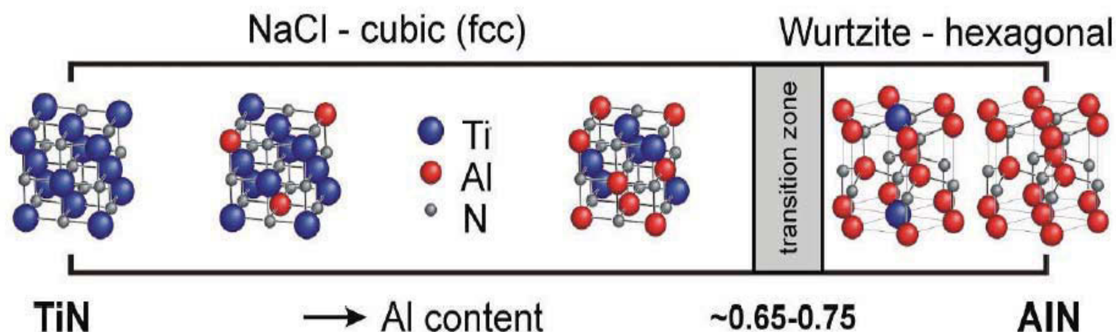

Fig. 3.3: Structural changes with increasing Al-content [28-29].

With increasing Al-content also the mechanical properties change significantly, as presented in Fig. 3.4b. The maximum hardness and Young's modulus are observed in coatings with am Al/(Ti+Al) ratio in the range of 0.5-0.6. Then the mechanical properties decrease drastically due to the formation of the wurtzite structure. This behaviour can be explained on the basis of bonding characteristics by Zhou et al. [31].

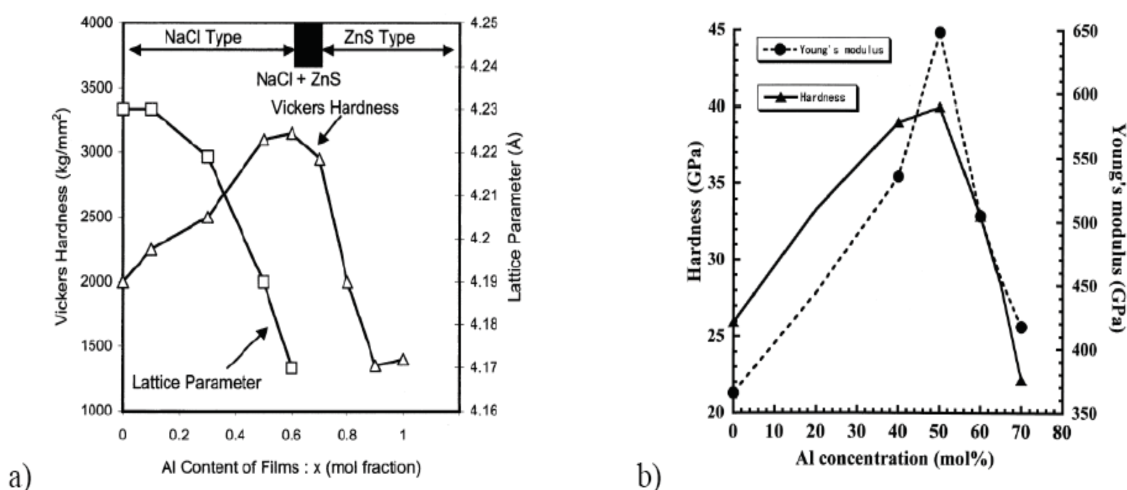

Fig. 3.4: a) Hardness and lattice parameter of $Ti_{1-x}Al_xN$ coatings as a function of Al-content. b) Hardness and Young's modulus of $Ti_{1-x}Al_xN$ coatings as a function of Al-content.

With increasing Al-content the mechanical properties of Nb-Al-N coatings as reported by R. Franz et al. [30], change significantly, see Fig. 3.5. The maximum hardness is observed in coatings with Al/(Nb+Al) ratio x of 0.45 at a bias potential of -40 V and for x = 0.27 at a bias potential of -120 V. The Young's Modulus decreased with increasing Al-content for both bias

potentials applied. The mechanical properties decrease drastically due to the formation of the wurtzite structure [30].

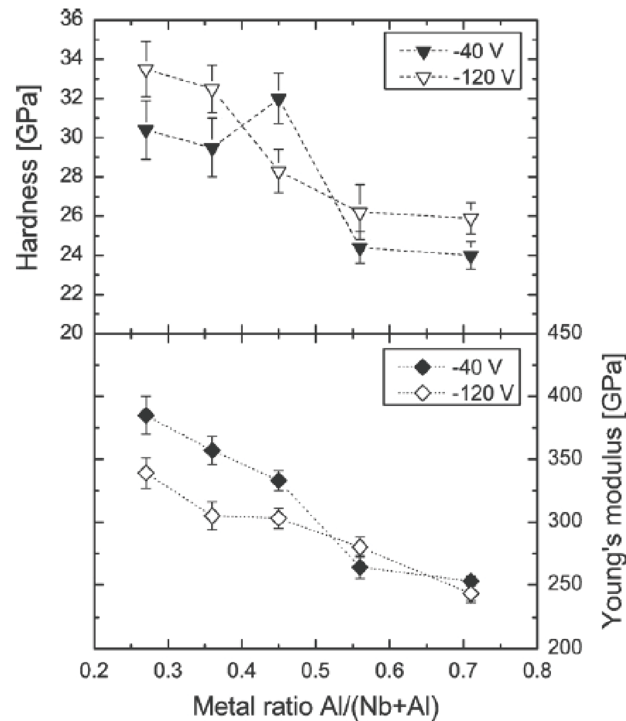

Fig. 3.5: Hardness and Young's modulus of $Nb_{1-x}Al_xN$ coatings as a function of Al-content [30].

Therefore, the major goal of this thesis was to investigate the chemical phase stability ranges within the binary systems Nb-N and Ta-N and the ternary systems Nb-Al-N and Ta-Al-N. The strategy was to vary the N_2 partial pressure during deposition of the Nb-N and Ta-N coatings. The obtained settings to prepare fcc-NbN and fcc-TaN where then used for the preperation of $Nb_{1-x}Al_xN$ and $Ta_{1-x}Al_xN$ by adding Al-platelets to the race trace of the respective Nb and Ta target.

4. Experimental

4.1 Film deposition

4.1.1 Deposition facility

All coatings investigated in this thesis were prepared by DC-reactive magnetron sputtering, using a modified Leybold-Heraeus A-400 magnetron sputtering unit, as presented in Fig. 4.1.

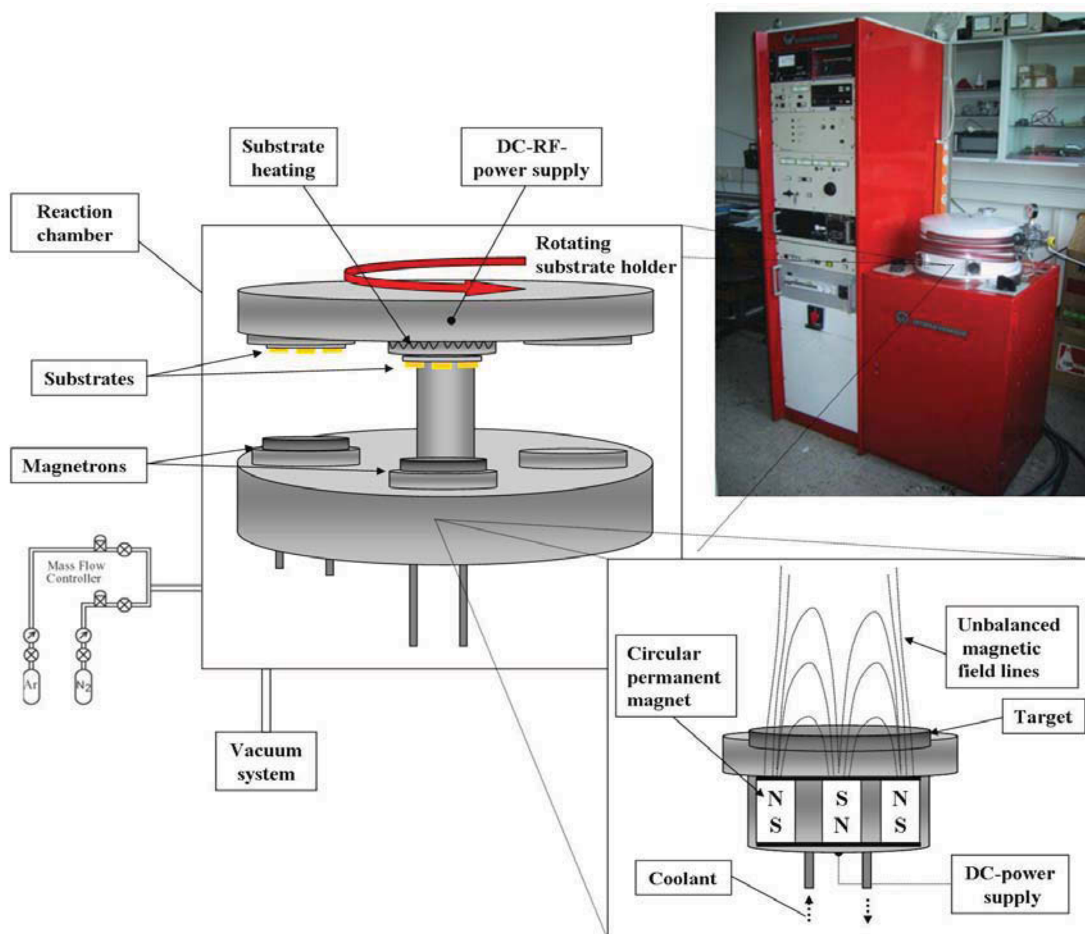

Fig. 4.1: Schematic drawing and photo of the lab-scale UBM-sputter plant [29].

The reaction chamber (Ø400*200 mm) consists of two parts. The upper part contains the rotateable substrate holder, while in the lower part the water cooled target positioned on a

circular unbalanced planar magnetron (Gencoa PK 75) is located. The two step pumping system consists of a rotary vane vacuum pump (Pfeiffer DUO 20) and a turbomolecular pump (Leybold Turbovac 361) in order to reach a base pressure of ~$3*10^{-3}$ Pa in the reaction chamber. To apply a negative potential for the substrate etching process, an independent RF-generator (ENI ACG-6B) was used. During the deposition process a negative potential was applied by a DC-bias generator (Sorensen DCR 300-1.5). Two gas flow control units (Tylan RO 7031, controller Tylan RO-7030) were used to adjust the working gas Ar flow up to 200 sccm and reactive gas N_2 flow up to 50 sccm, respectively. The measurement of the total pressure was done by a Leybold Combivac CM 31. During deposition, the sputter power was kept constant at 400 W and the voltage and current were automatically controlled by the Leybold-Heraeus DC power [32-36].

4.1.2 Targets and substrates

All coatings were deposited from high purity target materials as listed in Table 4.1. As mentioned earlier, the ternary coatings were prepared by the addition of Al-platelets on the target race track, as presented in Fig. 4.2. The Al-content in the coatings was varied by increasing the number of Al-platelets in the target, from 4 to 40, in steps of 4 platelets, respectively.

Table 4.1: Target materials.

Target	Purity[%]	Manufacturer
Nb (Ø = 75 mm, t = 6 mm)	99.9%	Plansee SE
Ta (Ø = 75 mm, t = 6 mm)	99.9%	Plansee SE
Al-Plates (Ø = 5 mm, t = 3 mm)	99.999%	Mateck

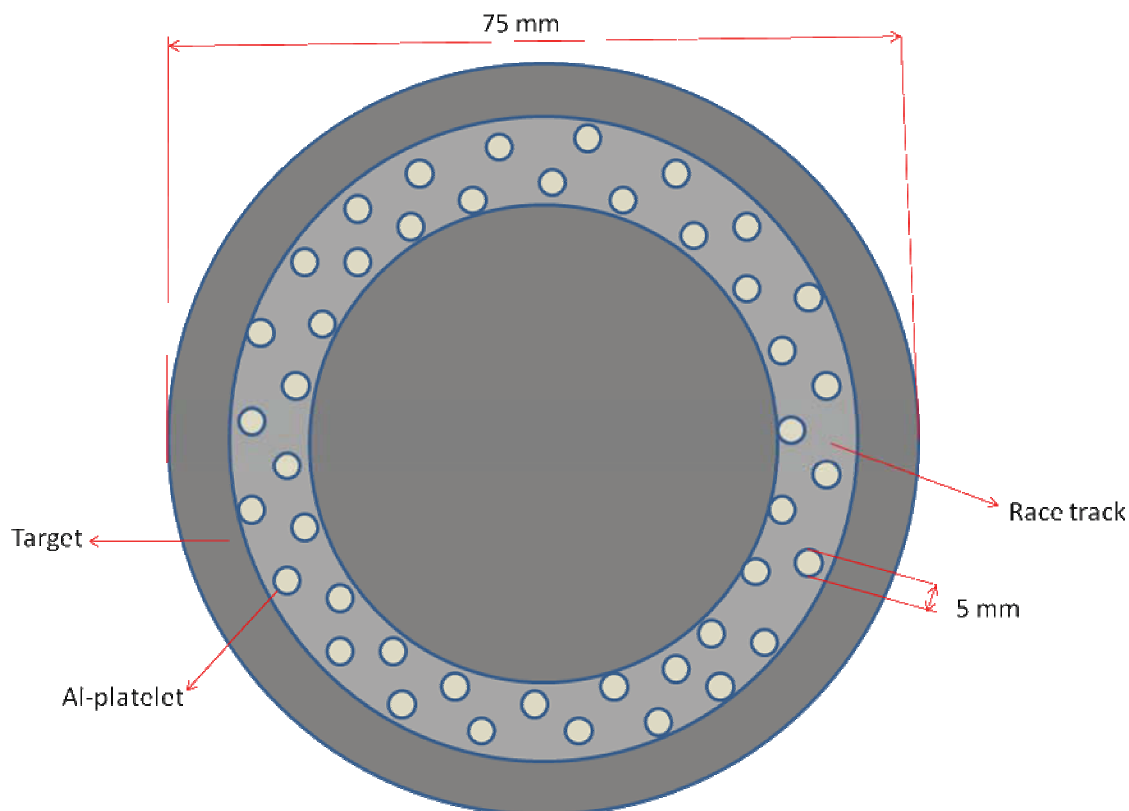

Fig. 4.2: Schematic drawing of the Al-platelet position on the Nb or Ta targets for the deposition of $Nb_{1-x}Al_xN$ and $Ta_{1-x}Al_xN$, respectively.

As the different investigation methods i.e., X-ray diffraction, nanoindentation and energy dispersive X-ray spectroscopy (EDX) required different substrates, the following two types of substrates are used as listed in Table 4.2:

Table 4.2: Substrate materials and main investigation.

Substrate	Investigation
Silicon Si (001)	Thickness and chemical investigation by EDX
Austenitic stainless steel	Structual investigation by XRD Nanoindentation

4.1.3 Deposition pre-cleaning

All coatings were deposited as follows:

a. Substrate preparation

The substrates were ultra sonically cleaned in aceton and ethanol for ~5 minutes, before being mounted on the substrate holder. During evacuation, the chamber wall was heated up to ~100 ^oC (outer heating) and the substrate heater was adjusted to 500 ^oC (internal heating) for 60 min. This baking procedures ensures desorption of adsorbed gas molecules on the chamber walls. After cooling for 45 min, a base pressure of $\leq 3*10^{-3}$ Pa was achieved. The substrate was heated up to 500 ^oC for 15 minutes, prior to deposition, to ensure the substrate being at sufficiently high temperature T_s for optimized growth conditions.

b. Deposition process

Sputter cleaning of the target was carried out by using 40 sccm argon and a power of 400 W for 5 minutes. In order to avoid contamination, the subtrates were rotated to the opposite side of the chamber, see Fig. 4.1. Subsequently, the target power was lowered to 80 W. Then the substrate etching was performed with 100 W using the RF-generator for 10 minutes, to clean the substrate surface prior to deposition, at a total pressure of ~$1.2*10^{-2}$ Pa.

After 10 minutes, the substrate was rotated back directly facing the target, and the RF-generator was turned off at the same time. The power was raised up to 400 W. For deposition of the binary coatings NbN_y and TaN_y, the argon flow was kept constant at 8 sccm, and nitrogen was introduced ranging from 2 sccm to 10 sccm corresponding to the variation of partial pressure (P_{N2}) between ~16 to 50%. This causes a total pressure P_T increase form 0.21 to 0.35 Pa. Then the total pressure was kept constant at P_T = 0.3 Pa and the partial pressure (P_{N2}) was increased from 60 to 100%.

The ternary coatings $Nb_{1-x}Al_xN$ and $Ta_{1-x}Al_xN$ were deposited at a constant total pressure of 0.30 Pa and 0.45 Pa, respectively.

The deposition time for the binary coatings was ranged from 30 up to 120 minutes, and for the ternary coatings a deposition time of 20 and 30 minutes was used, respectively.

4.2 Characterization

4.2.1 X-ray diffraction (XRD)

X-ray diffraction is a non-contact and non-destructive method to determine the lattice constants and crystallography of crystalline materials. Moreover, phase composition and orientation can be observed. This method is based on the diffraction of X-rays at crystallographic planes, according to Bragg's Law [37]:

$$n*\lambda = 2*d_{(hkl)}*\sin\theta \qquad (4.1)$$

n.....the order, λ.....the wavelength of the X-rays, $d_{(hkl)}$…..the lattice spacing with Miller indices (h,k,l) and θ…..the incident angle.

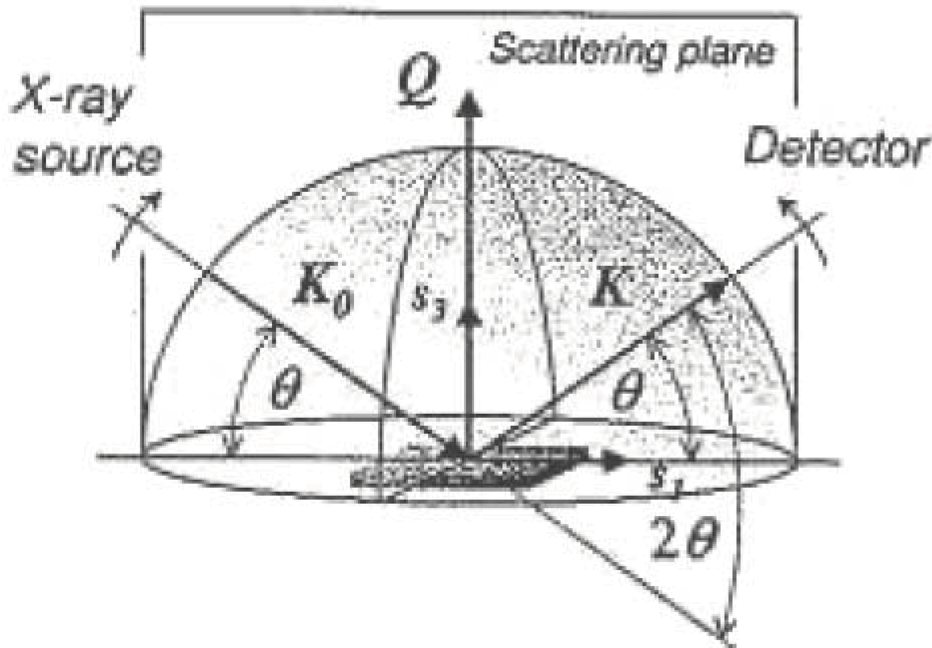

Fig. 4.3: Schematic θ-2θ scan mode by XRD [38].

Among different setups for diffraction analysis, the θ-2θ (Bragg-Brentano geometry) scan mode was used in this thesis, as shown in Fig. 4.3. The X-ray source moves with the angle θ, at the same time also the detector moves with θ, hence as compared to the source the detector moves with 2θ. The lattice spacing $d_{(h,k,l)}$ can be calculated from the XRD-pattern where constructive interference causes diffractions peaks at the 2θ angle position [38-39]. Therefore,

the coating structure can be identified by comparing it with data sheets from the Joint Committee on Powder Diffraction Standards (JCPDS) [55-56].

In this thesis a Siemens D500 Diffractometer was used, using Cu K_α radiation (λ = 1.54056 nm). The setup parameters are listed in Table 4.3:

Table 4.3: Parameters used for X-ray investigations.

Voltage[V]	Current[mA]	Step time[s]	Step[°]	2θ range[°]
40	25	1.2	0.02	30-120

4.2.2 Chemical analyses

Energy dispersive X-ray spectroscopy (EDX) attached to a scanning electron microscopy (SEM) was used to determine the chemical composition of the coatings. For more details see [40].

4.2.3 Coating thickness

The coating thickness is important for many further investigations. The measurements of the thickness was obtained by the so called Ball-Crater-Test, as presented in Fig. 4.4. During testing, the steel ball with a diameter D of 25 mm, covered by a diamond suspension rotates on the sample surface, and grinds a crater in to the coated steel sample. The thereby obtained inner diameter D_i and outer diameter D_o of the crater was measured by optical light microscopy, with an attached CCD camera.

The thickness t_c of the coating was then calculated according to Equation 4.2 [41]:

$$t_c = \frac{\left(D_0^2 - D_i^2\right)}{4D} \tag{4.2}$$

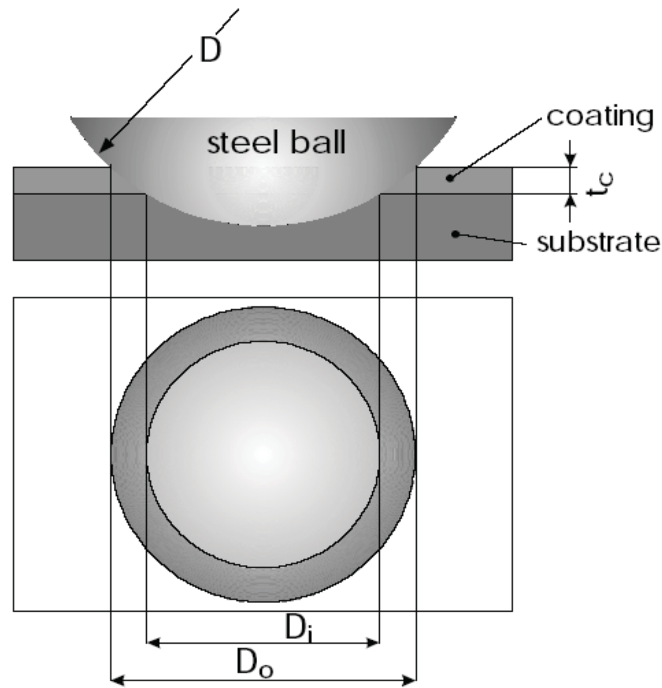

Fig. 4.4: Ball-Crater-Test in 2D drawing. [14,41]

4.2.4 Nanoindentation

The mechanical properties of the coatings, such as hardness and indentation modulus, are very important. The mechanical properties are very difficult to measure, because the coatings are very thin and very stiff. In the chapter 4.2.3, we have described the method to determine the thickness. The reason is that the hardness can be influenced by the substrate, when the indentation depth is above 10% of the coating thickness [42]. Therefore, the popular method for the determination of their mechanical properties is nanoindentation [43]. The UMIS Nanoindenter (Ultra Micro Indentation System) was used in this thesis, which is from Fischer-Cripps Laboratories [44]. A three-sided Berkovich indenter with a face angle of 65.27^{o} was used [45].

Figure 4.5 shows a typical load-displacement curve. The hardness can be calclulated by dividing the indentation force (P) by the contact area (A) [45]:

$$H = \frac{P}{A} \cdot \left(\frac{Ai}{A} \right) \tag{4.3}$$

Ai/A is the area ratio, which is applied to the results as a correction for the non-ideal indenter geometry.

The contact area A is calculated form the knowledge of the geometry of the tip and the indentation depth h_p.

The unloading curve is assumed to be elastic, even if the loading curve has a plastic deformation. From the slope of the unloading curve, which correlates with the stiffness (dP/dh), the elastic modulus can be calculated [45]:

$$E^* = \frac{dP}{dh} \frac{\sqrt{\pi}}{2\sqrt{A}} \sqrt{\frac{A_i}{A}} \tag{4.3}$$

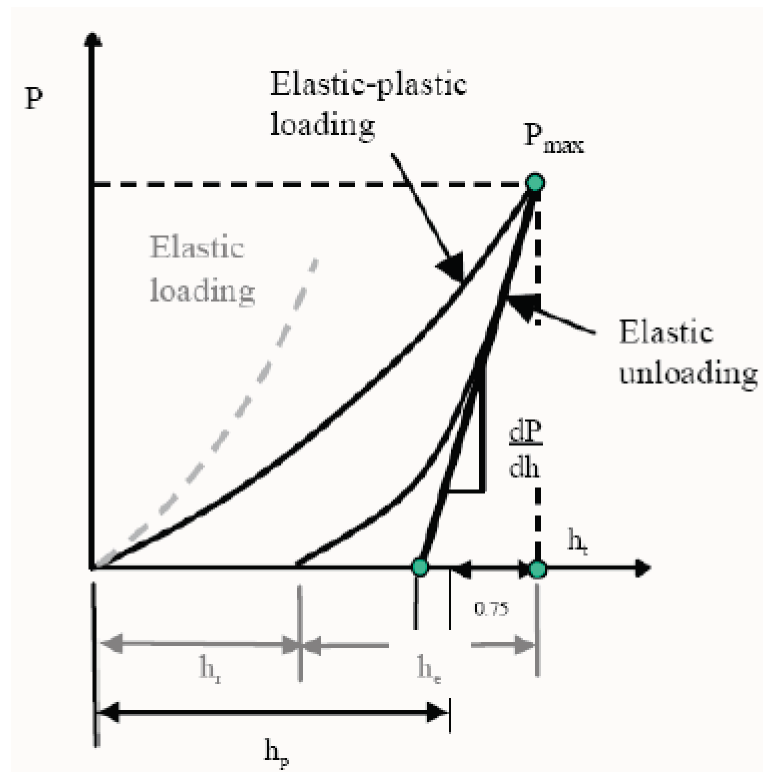

h_r…. residual indentation depth h_e….elastic indentation depth

h_p….contact indentation depth h_t….total indentation depth

Shape factor = 0.75.

Fig. 4.5: Schematic of a load-displacement curve [45].

Within this thesis, a plateau test was carried out with a maximum force of 18 mN and a minimal force of 8 mN with an increment of 0.5 mN. Considering statistics, 25 indents per coating were performed. Further on, the hardness and Young' modulus were calculated.

5 Results and discussion

5.1 NbN_y-thin films

5.1.1 Processing conditions and chemical compositions of NbN_y

The variation of N_2 gas flow during deposition, at constant Ar flow of 8 sccm, and increasing the N_2 flow from 2 to 10 sccm, is shown in Table 5.1. The increasing N_2 flow increases the total pressure (P_T) and N_2-partial pressure P_{N2}. All samples were deposited at T_s = 500 ^oC.

Table 5.1: Deposition parameters and chemical composition of NbN_y films deposited at varying total pressure.

Ar [sccm]	N_2 [sccm]	P_{N2}/ P_T [%]	P_T [Pa]	N/Nb
8	2	16	0.21	0.59
8	2.3	18	0.21	0.79
8	3	22	0.23	1.03
8	4	29	0.25	1.00
8	4.8	32	0.26	1.09
8	6	36	0.27	1.11
8	7.5	41	0.29	1.16
8	8	42	0.30	1.20
8	10	51	0.35	1.20

Table 5.2 shows the variation of Ar and N_2 gas flow during deposition while keeping the total pressure (P_T) constant. The increasing N_2 flow and decreasing Ar flow causes increasing N_2-partial pressure P_{N2}. All samples were deposited at T_s = 500 ^oC.

Table 5.2: Deposition parameters and chemical composition of NbN_y films deposited at constant $P_T = 0.3$ Pa.

Ar [sccm]	**N_2 [sccm]**	**P_{N2}/P_T [%]**	**P_T [Pa]**	**N/Nb**
8	8	42	0.30	1.20
5	11.5	60	0.30	1.28
4	14.2	70	0.30	1.36
2	16.1	80	0.30	1.33
1	18.2	90	0.30	1.30
0	20.2	100	0.30	1.12

5.1.2 Chemical composition of NbN_y

Increasing P_{N2}/P_T from 16% to 22% results in an increasing of N/Nb ratio from 0.59 to 1.03. A further increase from P_{N2}/P_T = 22% to 29% causes no significant change in the ratio. A further increase of P_{N2}/P_T from 29% to 51% causes an increase in N/Nb from 1 to 1.2. Increasing P_{N2}/P_T from 42% to 70% results in an increase of N/Nb ratio from 1.20 to 1.36. A continuous increase P_{N2}/P_T from 70% to 100% results in a decrease of N/Nb ratio from 1.36 to 1.12. Figure 5.1 nicely shows that the max N/Nb ratio of 1.36 is obtained with a N_2 partial pressure ratio of 70%.

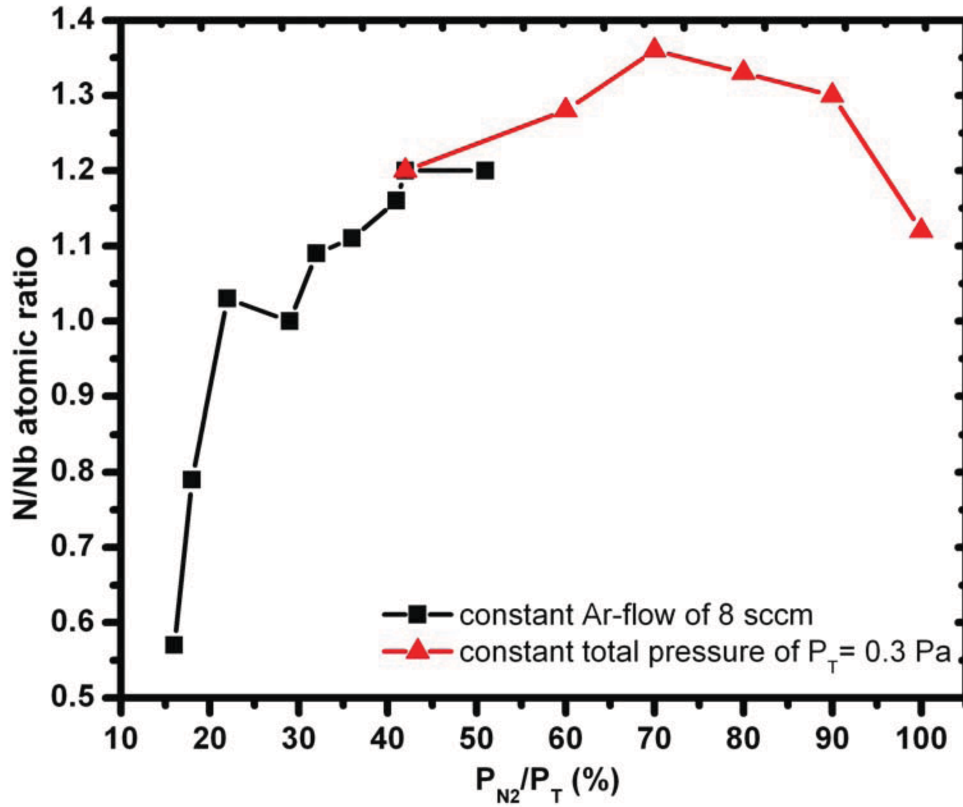

Fig. 5.1: N/Nb atomic ratio for NbN_y with increasing P_{N2}/P_T during deposition.

5.1.3 Growth rate of NbN_y

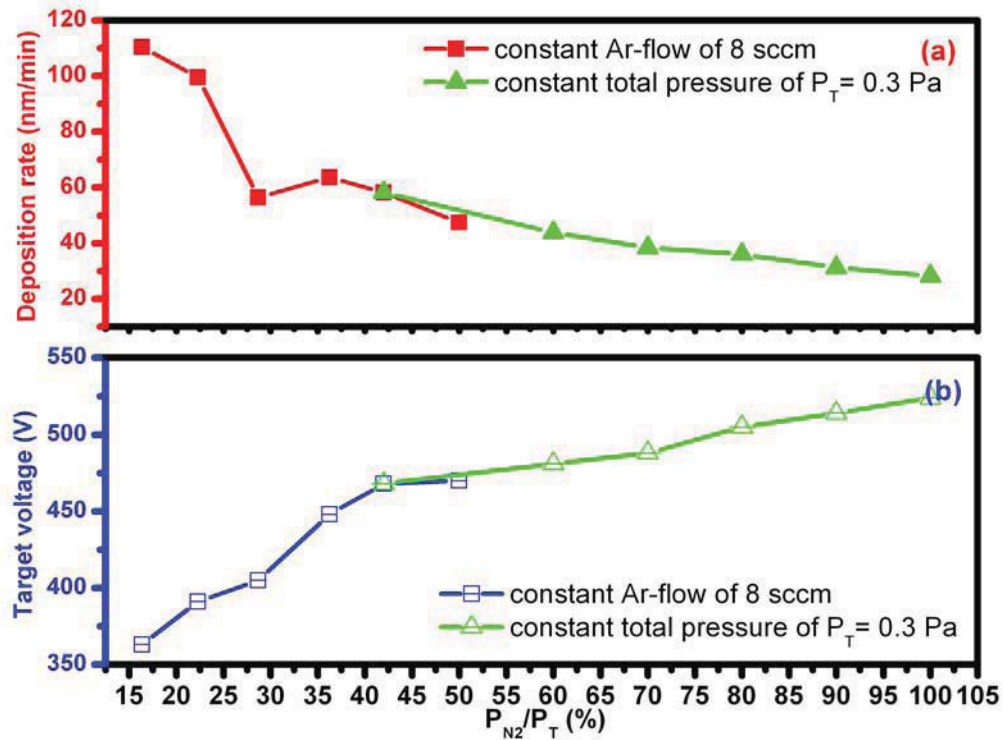

Fig. 5.2: (a) Growth rate and (b) target voltage for NbN_y with increasing P_{N2}/P_T.

With increasing P_{N2}/P_T from 16% to 29%, the deposition rate strongly decreases from 110 nm/min to 56 nm/min, as shown in Fig. 5.2a. This indicates a transition of the target surface from metallic to nitridic. While increasing P_{N2}/P_T to 51% the deposition rate only slightly decreases to 47 nm/min suggesting that the target is still in transition mode. The deposition rate can be explained by the increasing nitridic state of the target surface and the scattering loss due to the increased total pressure. The variation of the target voltage required, can be seen in Fig. 5.2b, and shows the same trend as more voltage is necessary for the nitrided target surface with increasing P_{N2}/P_T.

The deposition rate decreases with increasing of P_{N2}/P_T at a constant total pressure of 0.3 Pa, which is in agreement with our previous research, as seen in Fig. 5.2a. With increasing P_{N2}/P_T from 42 to 100% the deposition rate as well as the target voltage change almost linear with P_{N2}/P_T. This indicates that mainly the changed gas condition (from Ar + N_2 towards N_2) is responsible for the decrease of deposition rate or increase of the target voltage and the target surface is always nitrided.

5.1.4 XRD of NbN_y

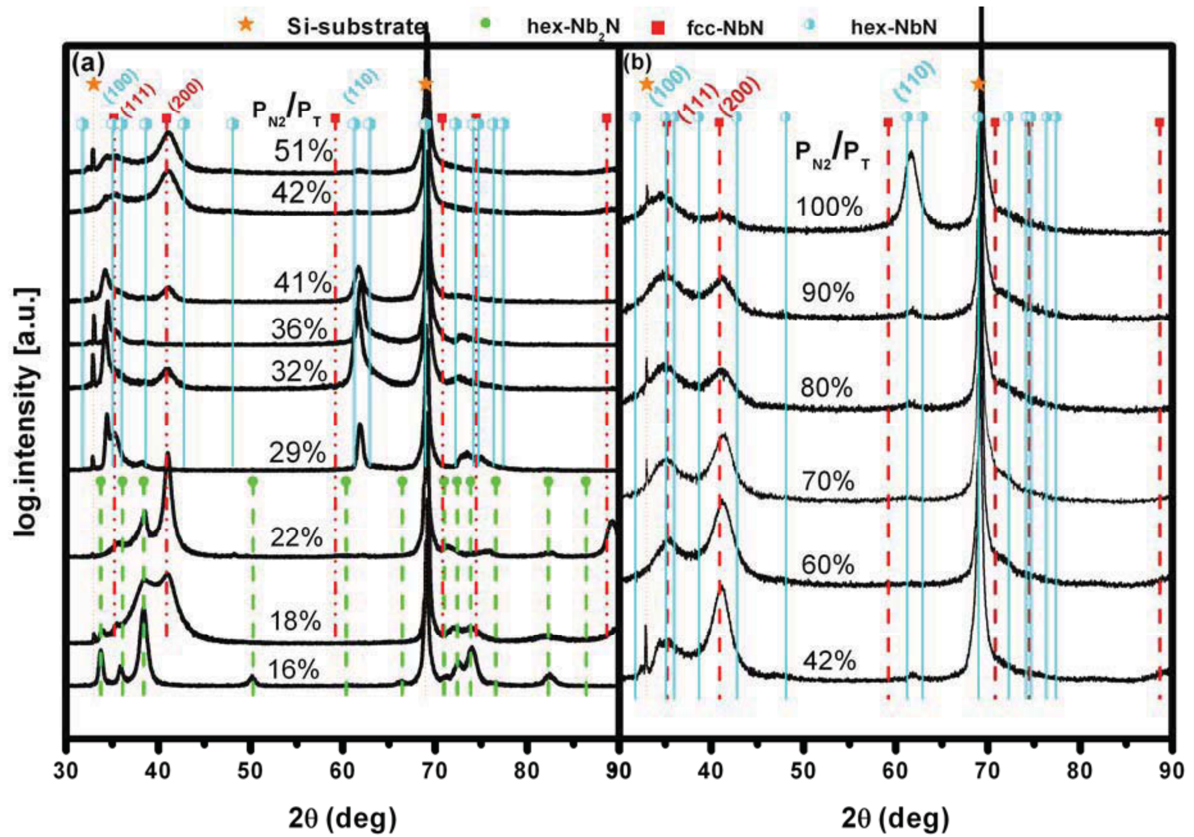

Fig. 5.3: XRD-patterns of as-deposited NbN_y-films with increasing P_{N2}/P_T during deposition (a) at varying total pressure and, (b) at constant $P_T = 0.30$ Pa.

The structure evolution of NbN_y is shown in Fig. 5.3a. XRD analysis shows that the films obtained with $P_{N2}/P_T = 16\%$ is composed of the hex-Nb_2N phase, which raughly corresponds to its chemical composition of $NbN_{0.57}$. The film grown with P_{N2}/P_T at 18%, corresponding to an N/Nb ratio of 0.79, exhibits a dual phase structure of hex-Nb_2N and fcc-NbN. Increasing P_{N2}/P_T from 22% to 29% results in an almost constant N/Nb ratio of ~1 and a transition of hex-Nb_2N into hex-NbN. Thus the films exhibit a mixed structure of hex-NbN and fcc-NbN. The films consist of a dual phase structure of fcc-NbN and hex-NbN, with increasing amounts of fcc-NbN with increasing of P_{N2}/P_T, until an almost single-phase fcc-NbN structure at $P_{N2}/P_T = 51\%$ is obtained.

All as deposited films exhibit over-stoichiometric nitrogen contents, and a two phase structure of fcc-NbN and hex-NbN, as given in Fig. 5.3b, when prepared at $P_T = 0.3$ Pa and varying P_{N2}/P_T from 42% to 100%. The dominating fcc-NbN structure exhibits mainly two strong

reflexes, e.g. (111) and (200) orientation. By increasing P_{N2}/P_T, the intensity of the (200) peak decreases, while the intensity of (111) peak increases and no significant change of the amont of the second phase (hex-NbN) can be observed. However, an increase of P_{N2}/P_T from 42% to 100% results in a change of the (111) orientation towards preferred (200) orientation at constant (small) amounts of the second phase (hex-NbN). A deposition in 100% N_2 results in a clearly defined two phase structure of fcc-NbN and hex-NbN, the content of hex-NbN increases from P_{N2}/P_T = 80% to 100%. At P_{N2}/P_T = 80% the (111) peak of fcc-NbN shift to the (100) peak of hex-NbN, and at P_{N2}/P_T = 100% a strong (110) peak of hex-NbN can be detected.

5.1.5 Mechanical properties of NbN_y

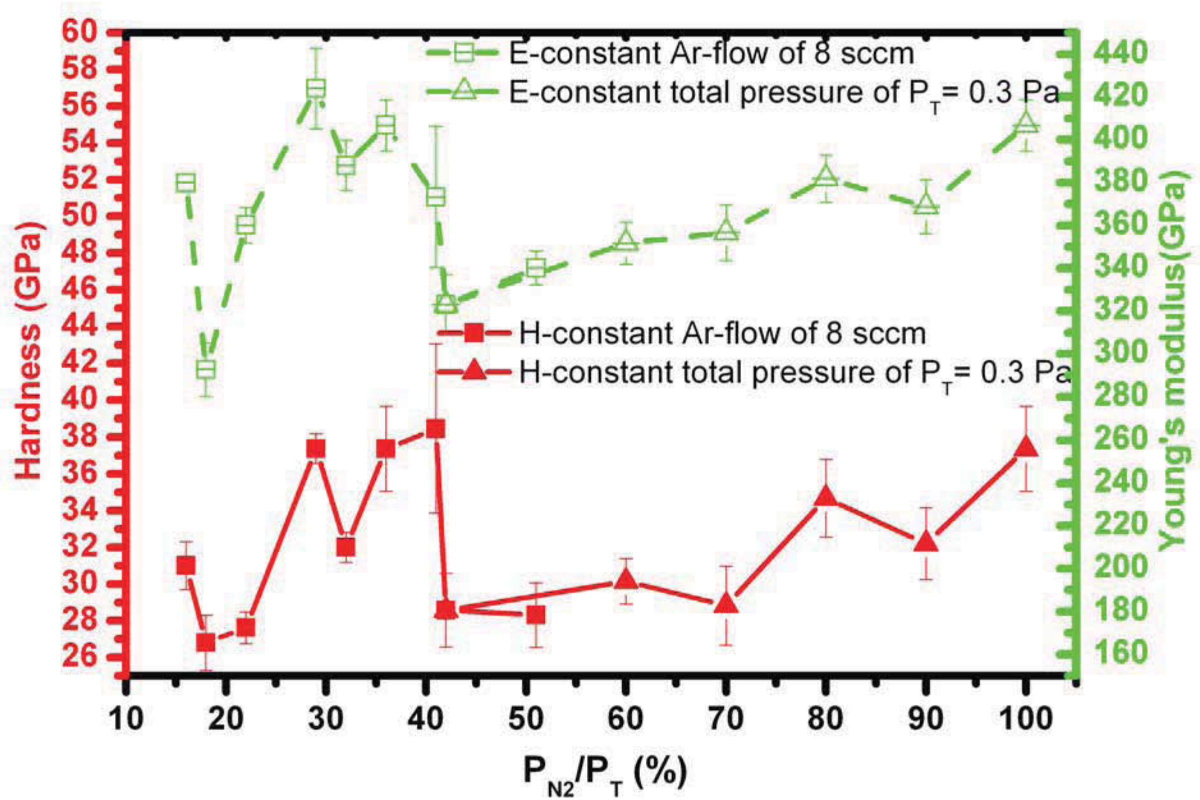

Fig. 5.4: Hardness and Young's modulus of NbN_y as a function of P_{N2}/P_T during deposition.

The obtained values for hardness (H) and Young's modulus (E) are presented as a function of N_2 partial pressure in Fig. 5.4. Both, the phase composition and structure play an important role for the observed mechanical properties. The single phase hex-Nb_2N coating (prepared at

P_{N2}/P_T = 16%) reaches a hardness ~31 GPa, which is in agreement to literature reports of Fontalvo et al. [46]. The appearance of a dual phase structure of hex-Nb_2N and fcc-NbN results in a hardness decrease to ~26.8 GPa. However, the structure transition into fcc-NbN and hex-NbN causes an increase in hardness to ~37.4 GPa. According to Sanjinés et al. [47], fcc-NbN has a low hardness value of ~25 GPa. Therefore, the hardness of deposited films with mixed fcc-NbN and hex-NbN phases for further increasing P_{N2}/P_T is. The variation of the indentation moduli E goes qualitatively along with the evolution of H as a function of P_{N2}/P_T, as can be seen in Fig.5.4 through the green open symbols.

The coatings contain two phases generated at high N_2-partial pressure from 42% to 100%, see Fig. 5.4, namely fcc-NbN and hex-NbN. It was shown that the hardness of fcc-NbN and hex-NbN are approximately ~28 GPa and ~38 GPa, respectively. Therefore, the two phase structure of P_{N2}/P_T = 100% including more hex-NbN, corresponds to a high hardness of ~37 GPa. A ratio of P_{N2}/P_T = 42% implies predominantly fcc-NbN, and therefore the corresponding hardness has a value of approximately ~28 GPa. The variation of Young's modulus E corresponds to the variation of hardness, see Fig. 5.4.

5.1.6 Comparsion of structures at over-stoichiometric compositions of N/Nb

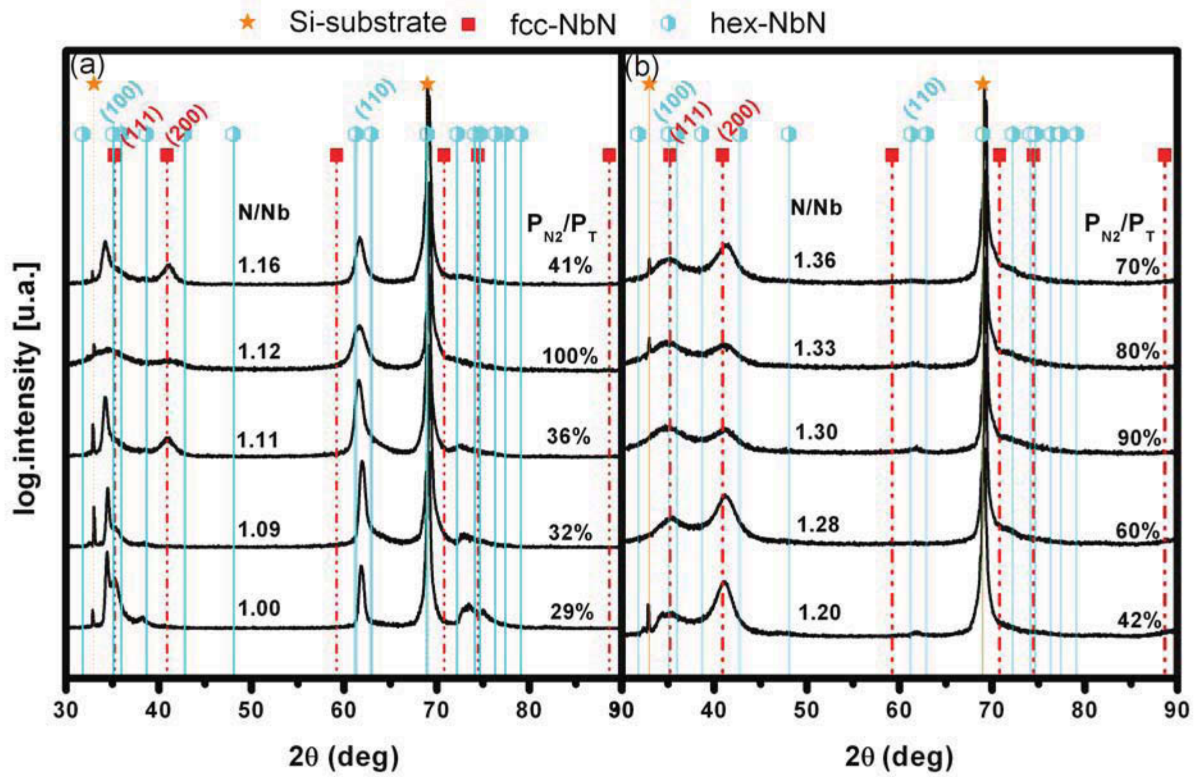

Fig. 5.5: XRD-patterns of as-deposited NbN_y-films with increasing N content (a) in the range from N/Nb=1.00 to 1.16 and, (b) in the range from N/Nb=1.20 to 1.36.

The phases of hex-NbN and fcc-NbN exist at over-stoichiometric compositions of N/Nb, as presented in Fig. 5.5. With increasing chemical composition of N/Nb from 1.00 to 1.16 an almost single phase hex-NbN with two strong orientations of (100) and (110) is obtained, see Fig. 5.5a. A further increase of N/Nb from 1.2 to 1.36 results in broader X-rays peaks and a shift towards fcc-NbN, see Fig. 5.5b.

5.1.7 Comparsion of mechanical properties at over-stoichiometric compositions of N/Nb

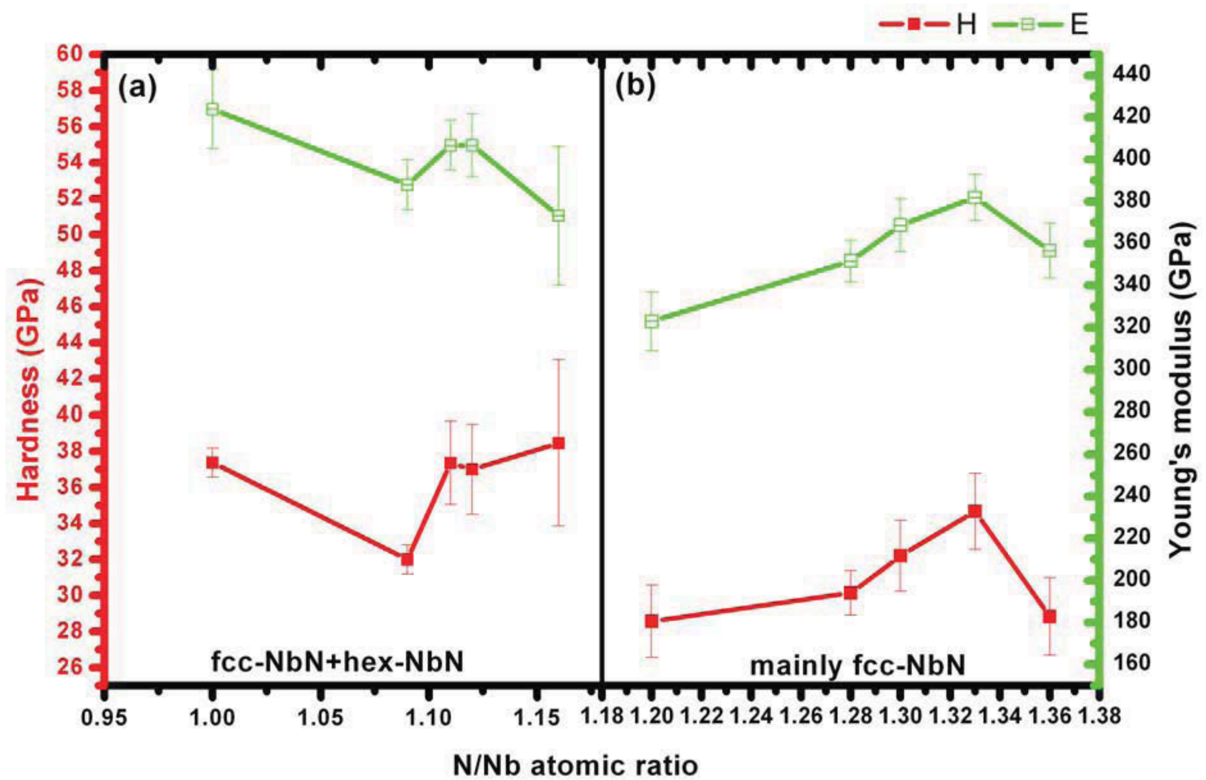

Fig. 5.6: Hardness and Young's modulus of as-deposited NbN_y-films with increasing N content (a) in the range from N/Nb = 1.00 to 1.16 and, (b) in the range from N/Nb = 1.20 to 1.36.

From the discussion in the previous section it is known that the structures change with increasing chemical composition at over-stoichiometric compositions of N/Nb. A similar variation between the hardness and Young's modulus variation and the variation of the concentration of the hex-NbN phase is observed as a function of the composition in the films, as presented in Fig. 5.6. It implies that the hardness and the Young's modulus values are governed by quantity of the hex-NbN in the film. Films with high concentration of the hex-NbN phase exhibit high hardness and Young's modulus. The hardness of the hex-NbN phase reaches ~38 GPa, whereas the hardness of the fcc-NbN is approximately ~28 GPa. The high hardness of ~34 GPa for the fcc-NbN dominated coatings Fig. 5.6b with N/Nb = 1.33 and ~32 GPa for N/Nb = 1.30 is mainly attributed to their small grain size as suggested by their broad XRD peaks, see Fig. 5.5b.

5.2 TaN_y- thin films

5.2.1 Processing conditions and chemical compositions of TaN_y

Table 5.3 shows the deposition parameters and chemical composition of TaN_y films during the deposition at a varying total pressure. As seen earlier at the deposition of NbN_y films, the N_2-partial pressure ratio P_{N2}/P_T was varied in the range of ~16% to ~51%, while keeping the Ar-flow constant at 8 sccm, consequently, the corresponding total pressure is changing in a range of ~0.21 to ~0.35 Pa.

Table 5.3: Deposition parameters and chemical composition of TaN_y films deposited at varying total pressure.

Ar [sccm]	N_2 [sccm]	P_{N2}/P_T [%]	P_T [Pa]	N/Ta
8	2	16	0.21	0.47
8	3	22	0.23	0.60
8	4	29	0.25	0.70
8	4.3	30	0.25	0.94
8	4.6	31	0.26	1.07
8	4.8	32	0.26	1.08
8	5	33	0.27	1.09
8	6	36	0.27	1.04
8	7	40	0.29	1.13
8	8	42	0.30	1.11
8	10	51	0.35	1.24

Table 5.4 shows the variation of Ar and N_2 gas flow during deposition while keeping the total pressure constant. Varying the P_{N2}/P_T causes a pronounced change in N/Ta ratio.

Table 5.4: Deposition parameters and chemical composition of TaN_y films deposited at constant $P_T = 0.3$ Pa.

Ar [sccm]	N_2 [sccm]	P_{N2}/P_T [%]	P_{total} [Pa]	N/Ta
8	8	42	0.30	1.11
5	11.5	60	0.30	1.35
4	14.2	70	0.30	1.25
2	16.1	80	0.30	1.35
1	18.2	90	0.30	1.61
0	20.2	100	0.30	1.46

5.2.2 Chemical composition of TaN_y

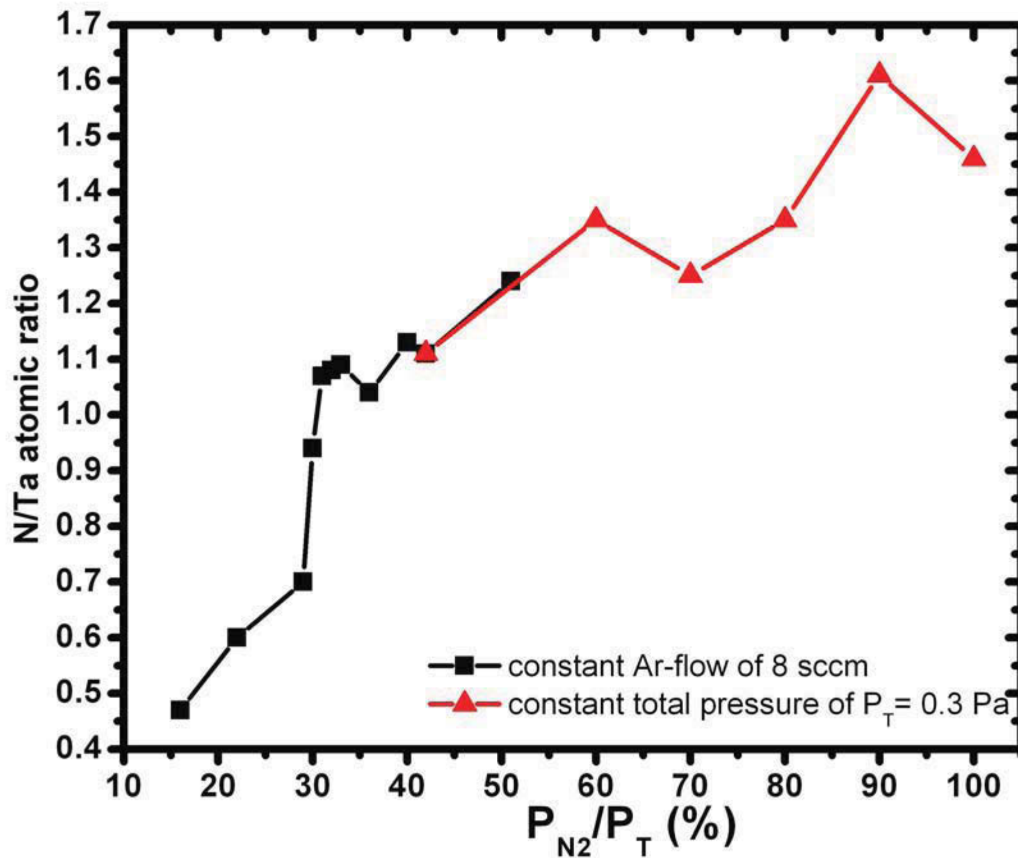

Fig. 5.7: N/Ta atomic ratio for TaN_y with increasing P_{N2}/P_T during deposition.

As shown in Fig. 5.7, varying P_{N2}/P_T causes a pronounced change in the N/Ta ratio. At low P_{N2}/P_T values, the film composition changes linearly from N/Ta = 0.47 with P_{N2}/P_T = 16% to N/Ta = 0.70 with P_{N2}/P_T = 29%. A further increase of N_2-flow from P_{N2}/P_T = 29% to 30% causes a significant change in the N/Ta ratio from 0.70 to 1.07, respectively. A further increase of P_{N2}/P_T to 51% causes a reduced increase of N/Ta from 1.04 to 1.24. Increasing P_{N2}/P_T from 42% to 90%, while keeping P_T at 0.30 Pa, results in an increase of N/Ta ratio from 1.11 to 1.61. Then, the N/Ta ratio decreases to 1.46 with 100% P_{N2}/P_T.

5.2.3 Growth rate of TaN_y

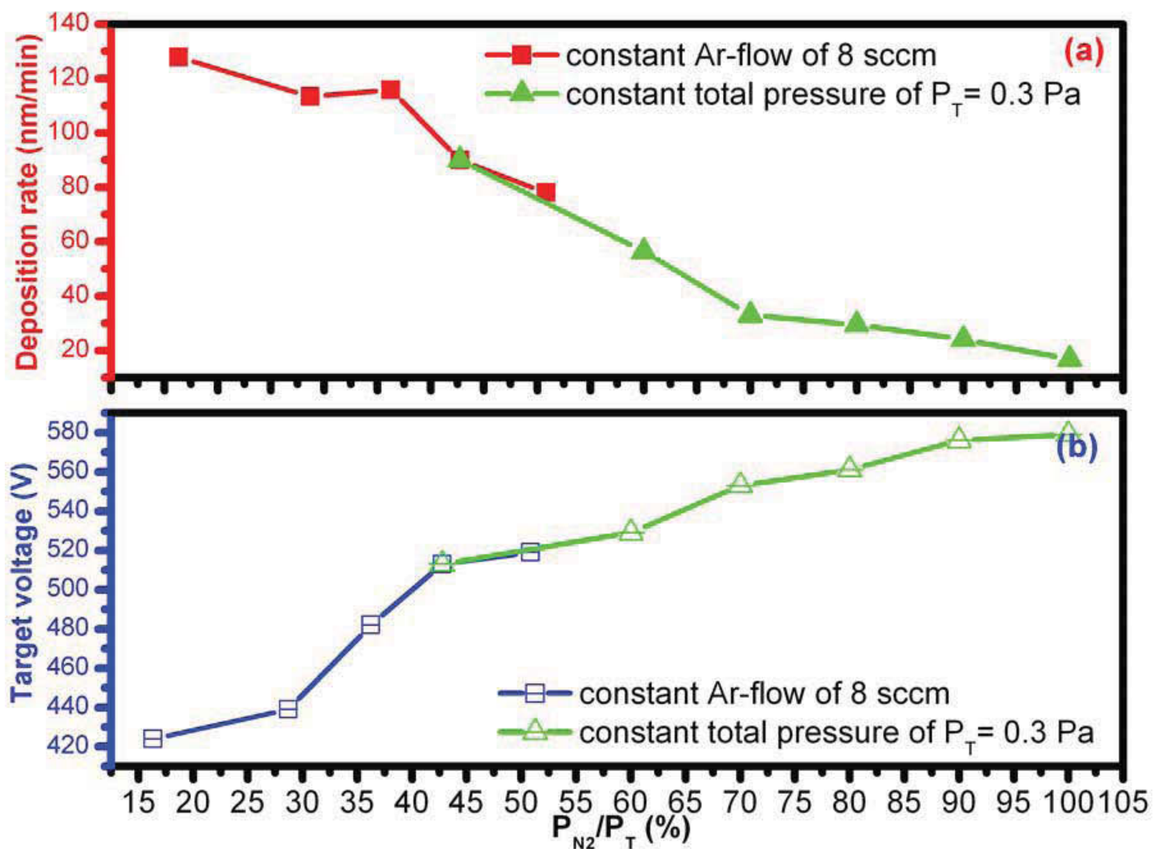

Fig. 5.8: (a) Growth rate and (b) target voltage for TaN_y with increasing P_{N2}/P_T.

Increasing P_{N2}/P_T from 16% to 51% at constant Ar flow and thus increasing total pressure induces a reduction in deposition rate from 130 to 80 nm/min, as shown in Fig. 5.8a. The N_2-partial pressure determines the degree of target nitridation and has a significant impact on the deposition rate. Comparison with the applied target voltage suggests that the target changes from metallic to transition mode up to the highest P_{N2} investigated.

The deposition rate decreases with increasing of P_{N2}/P_T at a constant total pressure of 0.3 Pa, as seen in Fig. 5.8a. A significant nitridation of the Ta target exhibit a decreasing deposition rate from 90 nm/min to 24 nm/min with increasing P_{N2}/P_T from 42 to 100%. The target voltage increases with increasing P_{N2}/P_T. The results suggest, that for $P_{N2}/P_T > 70\%$ the target is fully poisoned.

5.2.4 XRD of TaN_y

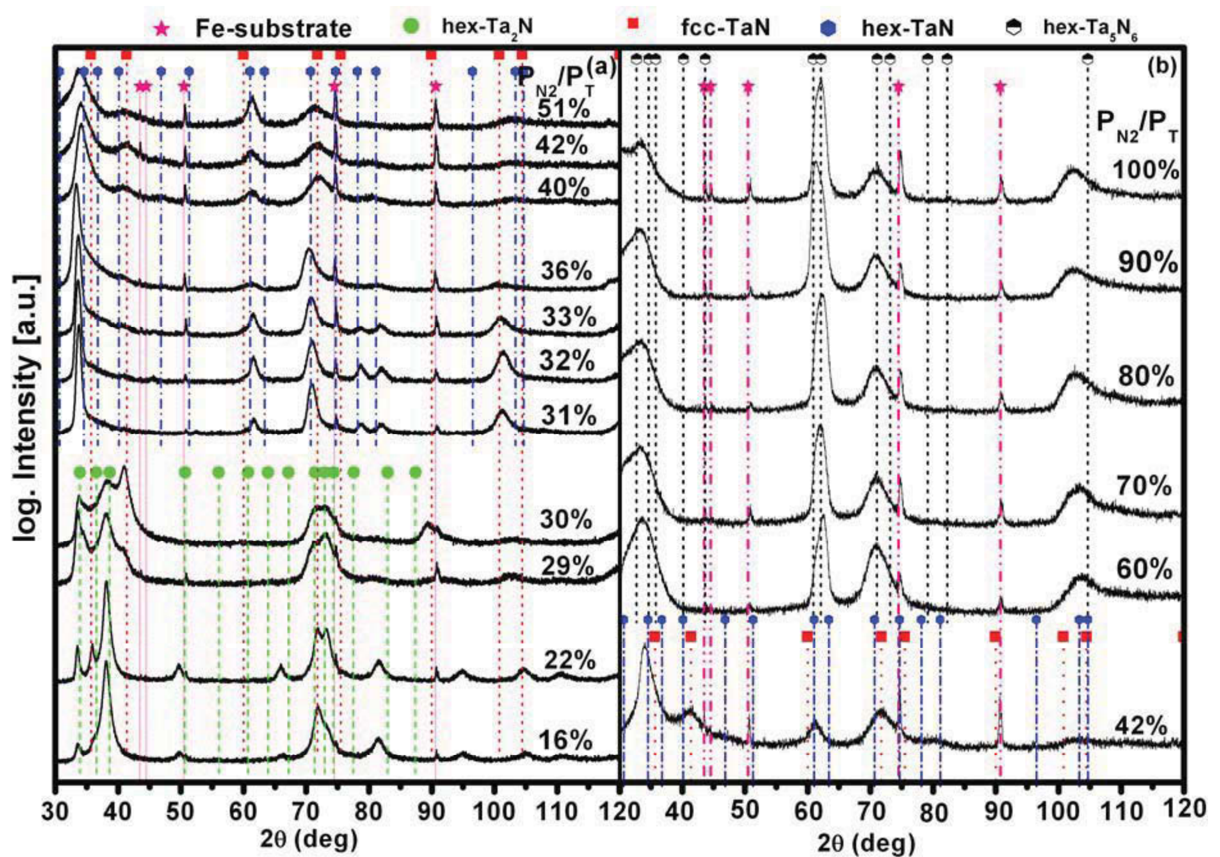

Fig. 5.9: XRD patterns for TaN_y-films with increasing P_{N2}/P_T during deposition (a) at varying total pressure and, (b) at constant P_T = 0.3 Pa.

The variation of P_{N2}/P_T induces a series of different structures as seen in Fig. 5.9a. XRD results showed that the films obtained at P_{N2}/P_T = 16% are composed of hex-Ta_2N, which corresponds to its chemical composition of $TaN_{0.47}$. Films grown at P_{N2}/P_T = 22%, correspond to a N/Ta ratio of 0.60, the structure shows a dual phase of hex-Ta_2N and fcc-TaN. Increasing P_{N2}/P_T from 29% to 30% shows a dual phase hex-Ta_2N and fcc-TaN with increasing the fcc-

TaN phase fraction, and the N/Ta ratio increases from 0.70 to 0.94. A further increase of P_{N2}/P_T from 31% to 51% results in a dual phase of fcc-TaN and hex-TaN.

All films deposited at constant total pressure P_T = 0.3 Pa and varying P_{N2}/P_T from 60% to 100% exhibit mainly hex-Ta_5N_6, see Fig. 5.9b.

The results are in good agreement to C.S. Shin [48]. With increasing P_{N2}/P_T the phases transformed from hex-Ta_2N to hex-Ta_2N+fcc-TaN and further to fcc-TaN, when using a substrate temperature below 650 ^oC. With higher substrate temperatures the films exhibit at high P_{N2}/P_T a two phase structure composed of fcc-TaN+hex-TaN. G.R. Lee has reported that also with increasing ion energy (E_i) the structures of TaN_y films transformed from fcc-TaN to a lamellar structure composed of fcc-TaN+hex-TaN or fcc-TaN+hex-Ta_2N [49].

5.2.5 Mechanical properties of TaN_y

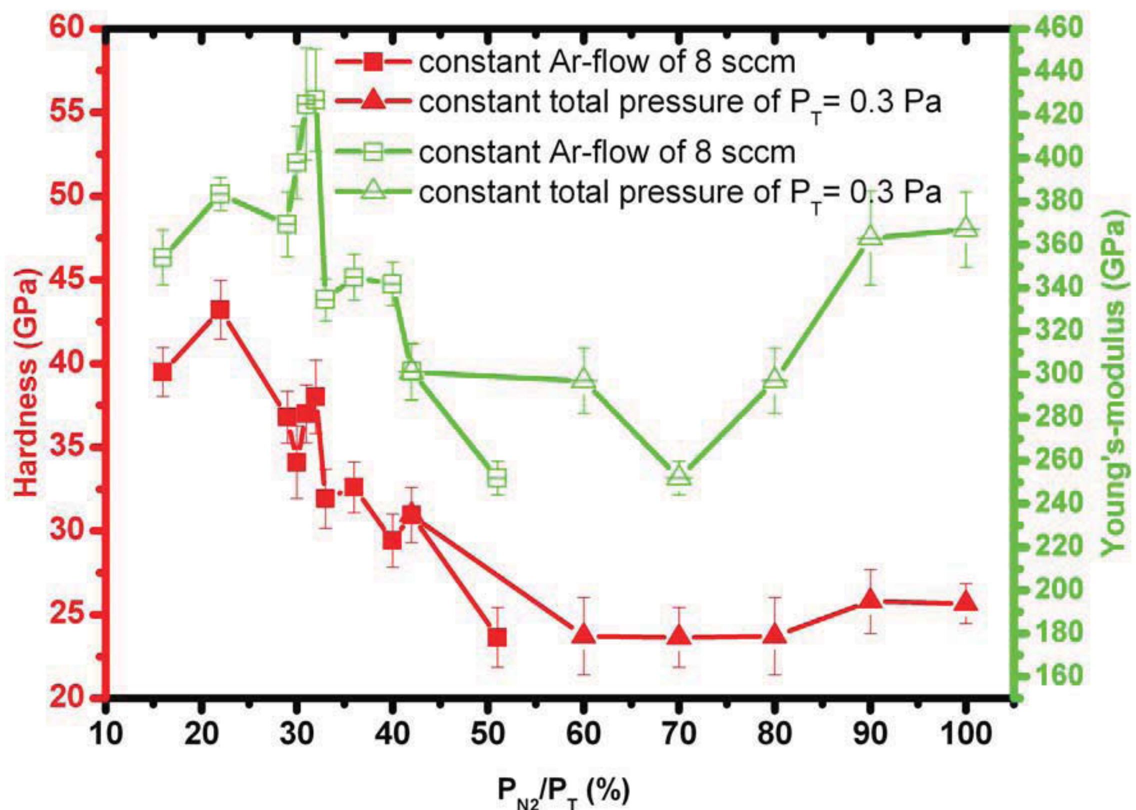

Fig. 5.10: Hardness and Young's modulus of TaN_y as a function of P_{N2}/P_T during deposition.

The obtained nanoindentation values for hardness H and Young's modulus E of the deposited films are presented as a function of N_2-partial pressure in Fig. 5.10. The mechanical properties

strongly correlate with the microstructure. The predominantly hex-Ta_2N coating prepared at P_{N2}/P_T = 16% exhibit a hardness of 39.5 GPa. Corresponding to the increasing P_{N2}/P_T to 22%, a dual phase of hex-Ta_2N and fcc-TaN was obtained, and the hardness is increasing as well up to ~43 GPa. This behavior is explained by G.R. Lee, el at., who showed that the hardness increased from 21.1 to 45.5 GPa with increasing ion energy, as thereby a self-organized lamellar structure is obtained. This structure consists of hex-Ta_2N and fcc-TaN or fcc-TaN and hex-TaN in a multilayer arrangement [50]. The hardness decreases with a higher content of fcc-TaN. This results in this thesis show that a further increasing P_{N2}/P_T from 31% to 36% results in a dual phase of hex-TaN and fcc-TaN. Due to the multilayer effect the hardness is still very high with ~38 GPa. Then an increasing P_{N2}/P_T to 42% results in a higher content of fcc-TaN and the hardness decreases to ~29 GPa.

The structure of the TaN_y-films prepared with P_{N2}/P_T = 40% is composed of hex-TaN and fcc-TaN, with a hardness of ~31 GPa. As with a further increase of P_{N2}/P_T from 60% to 100% is composed of hex-Ta_5N_6, with a constant lower hardness of ~24-25 GPa, see Fig. 5.10. The modulus E increase rapidly with increasing ratio of N/Ta from 70% to 90%, and then keeping constant at higher ratio of N/Ta. This behavior can be explained by the generated cracks of the coatings, see Fig. 5.11. This crack-formation definitely influences the nanoindentation measurements.

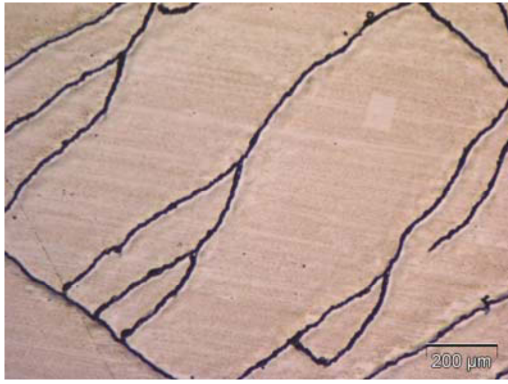

(a) P_{N2}/P_T = 60%, N/Ta = 1.35

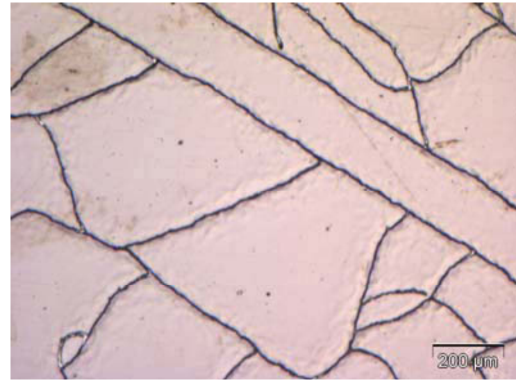

(b) P_{N2}/P_T = 70%, N/Ta= 1.25

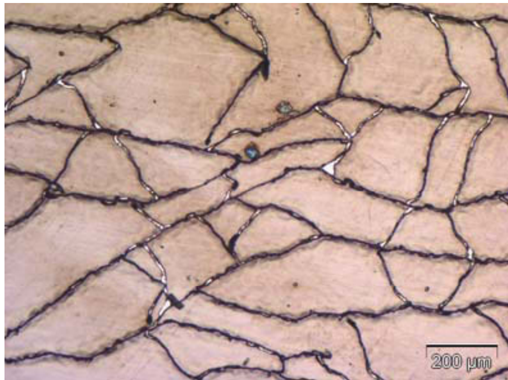

(c) P_{N2}/P_T = 80%, N/Ta = 1.35

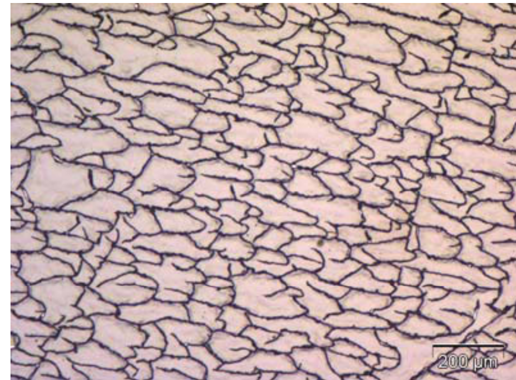

(d) P_{N2}/P_T = 90%, N/Ta = 1.61

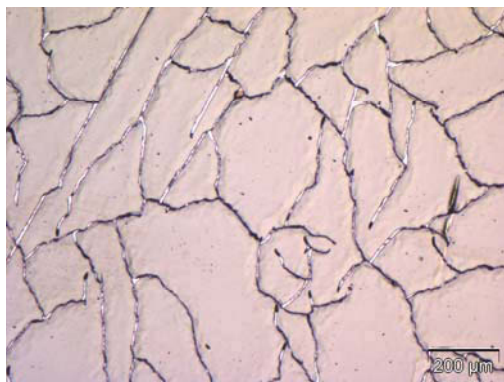

(e) P_{N2}/P_T = 100%, N/Ta = 1.46

Fig. 5.11: Different cracks on the surface of as-deposited TaN_y-films with increasing P_{N2}/P_T (a) P_{N2}/P_T = 60%, N/Ta = 1.35 (b) P_{N2}/P_T = 70%, N/Ta = 1.25 (c) P_{N2}/P_T = 80%, N/Ta = 1.35 (d) P_{N2}/P_T = 90%, N/Ta = 1.61 (d) P_{N2}/P_T = 100%, N/Ta = 1.46.

5.2.6 Comparsion of structures at over-stoichiometric compositions of N/Ta

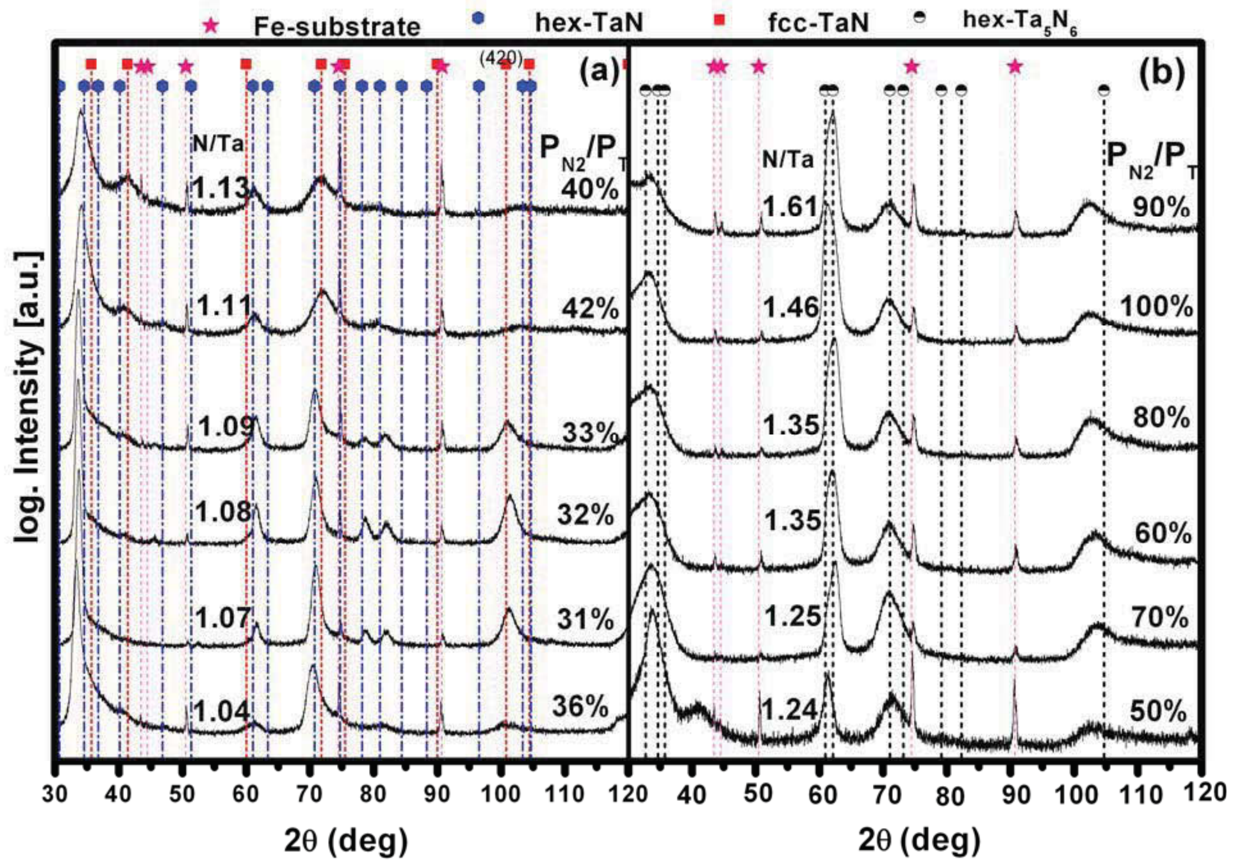

Fig. 5.12: XRD-patterns of as-deposited TaN_y-films with increasing N-content (a) in the range from N/Ta = 1.04 to 1.13 and, (b) in the range from N/Ta = 1.24 to 1.61.

With increasing chemical composition of N/Ta from 1.04 to 1.09 a dual phase of fcc-TaN and hex-TaN exists. In this area peaks corresponding to the phase of hex-TaN and a significant (420) peak of fcc-TaN can observed. A further increase of N/Ta from 1.11 to 1.13 leads also to a dual phase of fcc-TaN and hex-TaN. This dual phase consists of high fcc-TaN phase content, as shown in Fig. 5.12a. Increasing the N/Ta composition further from 1.24 to 1.61 results in a hex-Ta_5N_6 phase, see Fig. 5.12b.

5.1.7 Comparsion of mechanical properties at over-stoichiometric compositions of N/Ta

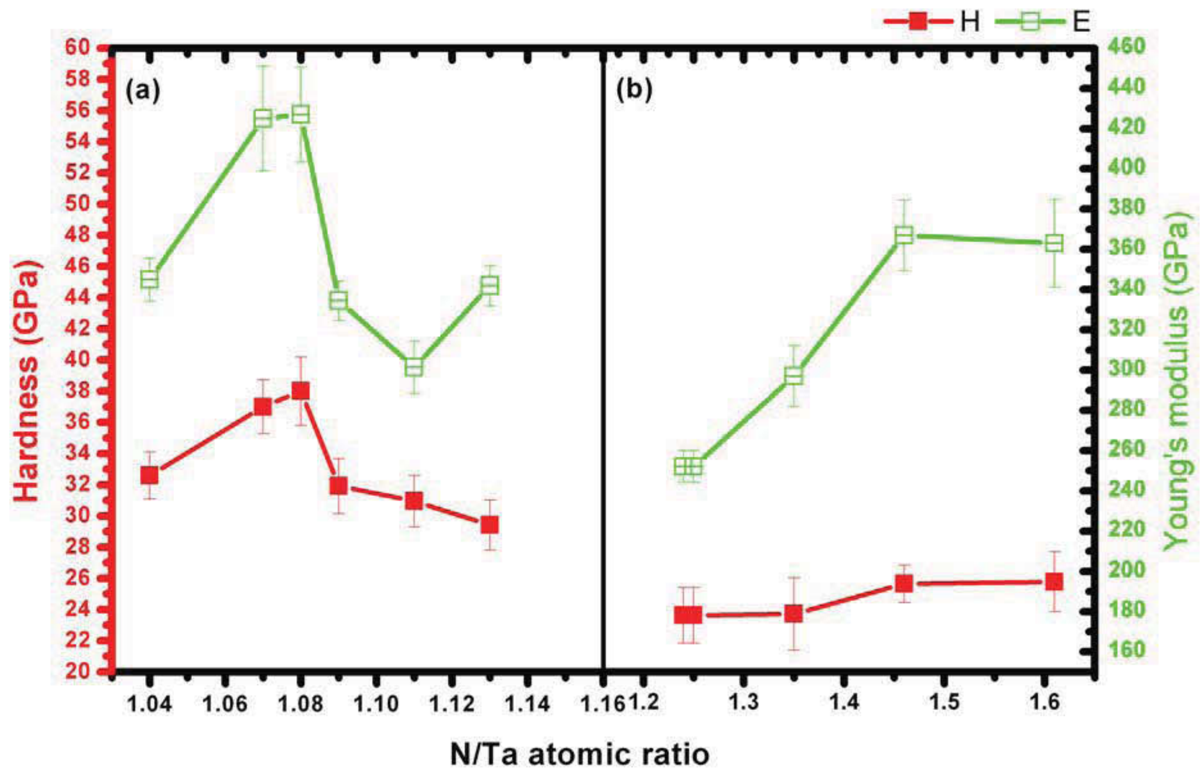

Fig. 5.13: Hardness and Young's modulus of as-deposited TaN_y-films with increasing N content (a) in the range from N/Ta = 1.04 to 1.13 and, (b) in the range from N/Ta = 1.24 to 1.61.

As presented in Fig. 5.13a, with increasing N/Ta from 1.04 to 1.08 the hardness value increases from ~ 33 GPa to ~ 38 GPa, due to the multilayer effect, as mentioned earlier. A further increase of N/Ta from 1.08 to 1.13 leads to a decrease of the hardness value from ~38 GPa to ~29 GPa, which is consistent with the increase of the fcc-TaN phase. Therefore, the hardness values of fcc-TaN can be implied of ~ 29 GPa. A further increase of N/Ta from 1.24 to 1.61 leads to an almost single phase of hex-Ta_5N_6, with a low hardness of ~24-25 GPa, see Fig. 5.13b. These coatings exhibit a pronounced crack formation.

5.3 $Nb_{1-x}Al_xN$-thin films

5.3.1 Processing conditions and chemical compositions of $Nb_{1-x}Al_xN$

$Nb_{1-x}Al_xN$ films were deposited onto Si substrates, reaching chemical compositions as presented in Table 5.5 by adding Al-platelets to the Nb-target as described in chapter 4.1.2, Fig. 4.2. Chemical analysis by EDX reveals that the elements in $Nb_{1-x}Al_xN$ films are over-stoichiometric with respected to their nitrogen content (N/metal ratios of 1.13-1.28, see Table 5.5). The Al content x of the deposited $Nb_{1-x}Al_xN$ films increases from x = 0.11 to 0.70 with increasing the numbers of Al platelets on the target.

Table 5.5: Chemical composition of the deposited films and used numbers of Al platelets on the Nb-target during deposition with P_T = 0.30 Pa, P_{N2}/P_T = 42%, T_s = 500 ^oC, and V_b = -50 V.

Coating	Al-platelets	Nb [at.%]	Al [at.%]	N [at.%]	N/(Al+Nb)	Al/(Al+Nb)
NbN	0	45.57	0	54.43	1.20	0
$Nb_{0.89}Al_{0.11}N$	4	39.94	4.77	55.29	1.24	0.11
$Nb_{0.81}Al_{0.19}N$	8	36.35	8.43	55.22	1.23	0.19
$Nb_{0.68}Al_{0.32}N$	12	29.84	13.93	56.23	1.28	0.32
$Nb_{0.58}Al_{0.42}N$	16	27.45	19.53	53.02	1.13	0.42
$Nb_{0.57}Al_{0.43}N$	20	26.18	19.41	54.41	1.19	0.43
$Nb_{0.56}Al_{0.44}N$	24	24.75	19.38	55.88	1.27	0.44
$Nb_{0.44}Al_{0.55}N$	28	19.89	24.83	55.28	1.24	0.55
$Nb_{0.39}Al_{0.61}N$	32	17.53	27.55	54.92	1.22	0.61
$Nb_{0.34}Al_{0.66}N$	36	15.12	28.87	56.00	1.27	0.66
$Nb_{0.30}Al_{0.70}N$	40	13.07	30.77	56.16	1.28	0.70

5.3.2 Colours of $Nb_{1-x}Al_xN$

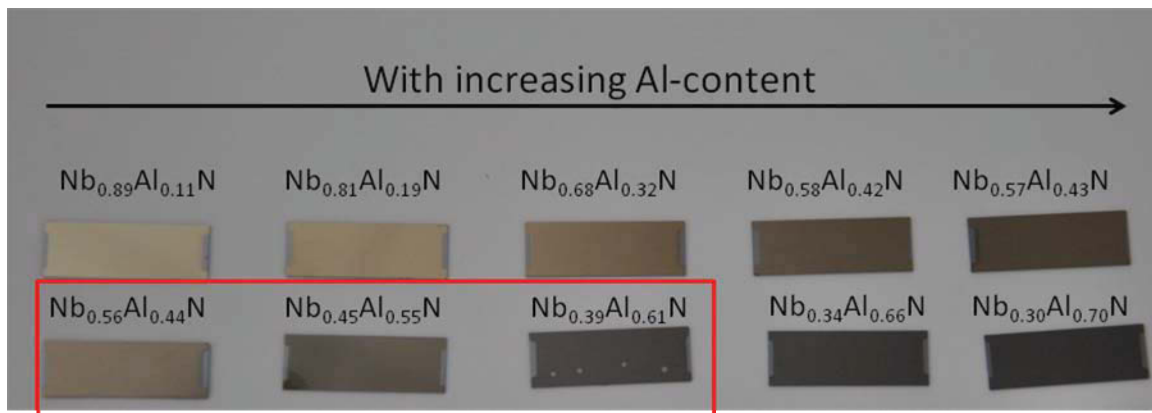

Fig. 5.14: Different colours with increasing Al-content of the $Nb_{1-x}Al_xN$ coatings.

The colour of the $Nb_{1-x}Al_xN$ coatings changes from golden to grey to dark grey with increasing Al content, as seen in Fig. 5.14. Until x = 0.44 the golden colour dominates. Focusing on the $Nb_{0.56}Al_{0.44}N$, $Nb_{0.45}Al_{0.55}N$, $Nb_{0.39}Al_{0.61}N$ coatings, highlighted by a red rectangle, the colour change clearly from golden to grey to dark grey. The $Nb_{0.45}Al_{0.55}N$ film indicates the transition from gold to grey. Further increasing the Al content from x = 0.61 to 0.70 keeps the colour metallic grey.

5.3.3 Phases of $Nb_{1-x}Al_xN$

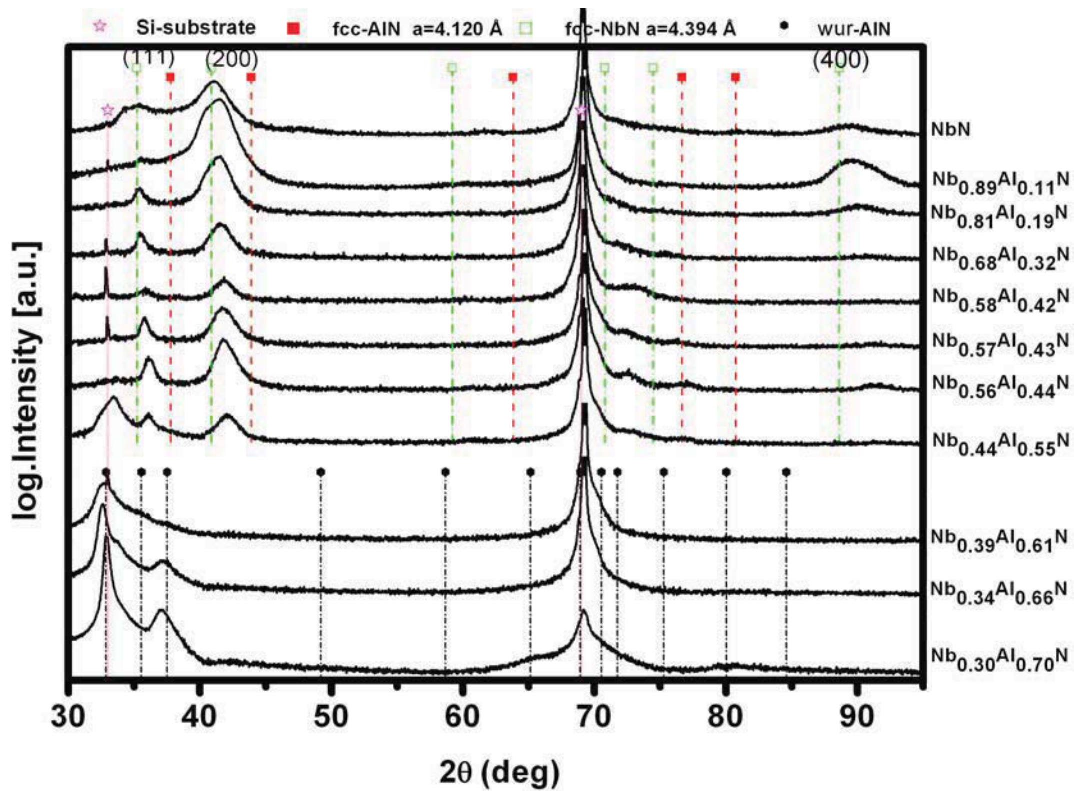

Fig. 5.15: XRD patterns of $Nb_{1-x}Al_xN$ coatings.

The $Nb_{1-x}Al_xN$ films exhibit a single-phase B1 NbN structure up to Al contents of x = 0.44, as shown in Fig. 5.15. The diffraction peaks shift to higher angles due to the substitution of Nb atoms by Al-atoms, which are smaller. However, Selinder et al. reported that Nb-Al-N films with Al contents of x = 0.50 at the metal sublattice exhibit a single-phase cubic structure when using a T_s of 500 ^oC and a total pressure of $P_T = 2$ Pa [50]. From Fig. 5.15 it can be seen that the (111)/(200) reflex intensity increases with increasing Al content. A further increase of Al mole fraction x results in a structural transition into a mixed cubic-hexagonal structure, see Fig. 5.15 for x = 0.55. Finally, the films exhibit a single-phased hexagonal structure for $x \geq 0.61$.

5.3.4 Lattice parameters of $Nb_{1-x}Al_xN$

(a)

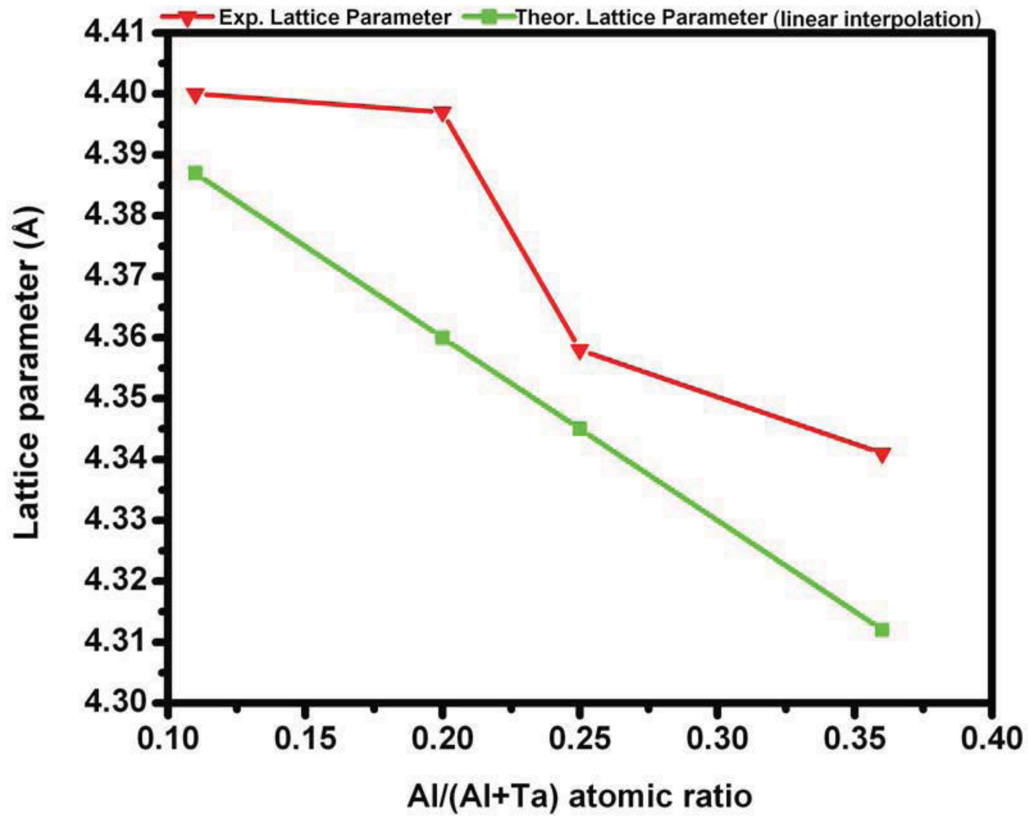

(b)

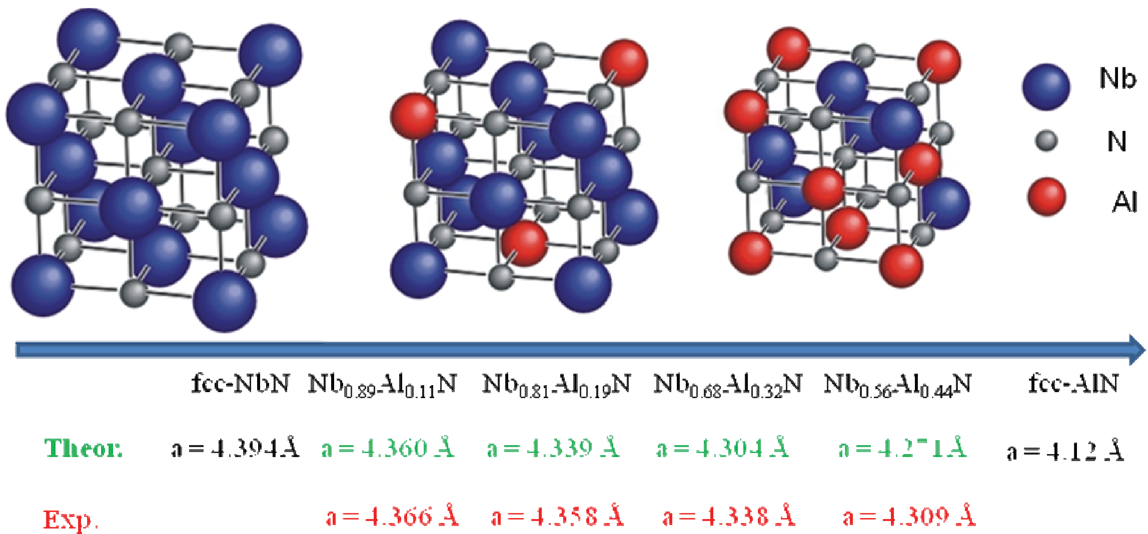

Fig. 5.16: (a) Lattice parameter of $Nb_{1-x}Al_xN$ as a function of Al-content. (b) Schematic representation of the solid-solution in a fcc-$Nb_{1-x}Al_xN$ crystal.

The determination of the lattice parameter for the Al-containing films was achieved by using the Cohen-Wagner method [51].

The theoretical lattice parameter was calculated using Vegard's rule, where a linear change of the lattice parameter with composition is assumed, see Fig. 5.16b. The theoretical lattice parameter are obtained by a linear interpolation between NbN (a = 4.394 Å) and AlN (a = 4.12 Å), which corresponds to Vegard' rule [53].

To further describe the deviation from Vegrad's rule, following formula is used:

$$a(x) = xa_{NbN} + (1-x)a_{AlN} + \delta x(1-x) \tag{5.1}$$

where a(x) is the experimental lattice constant of the $Nb_{1-x}Al_xN$ film, a_{NbN} and a_{AlN} are the lattice parameters of the boundary systems from JCPDS Card Nos. 00-038-1155 and Nos.00-025-1495, respectively, and δ is the deviation parameter [52].

The observed behavior reaches values of δ = 0.031,0.110,0.149,and 0.147 Å for Al content x = 0.11 at to 0.19 to 0.32 to 0.44, respectively.

5.3.5 Growth rate of $Nb_{1-x}Al_xN$

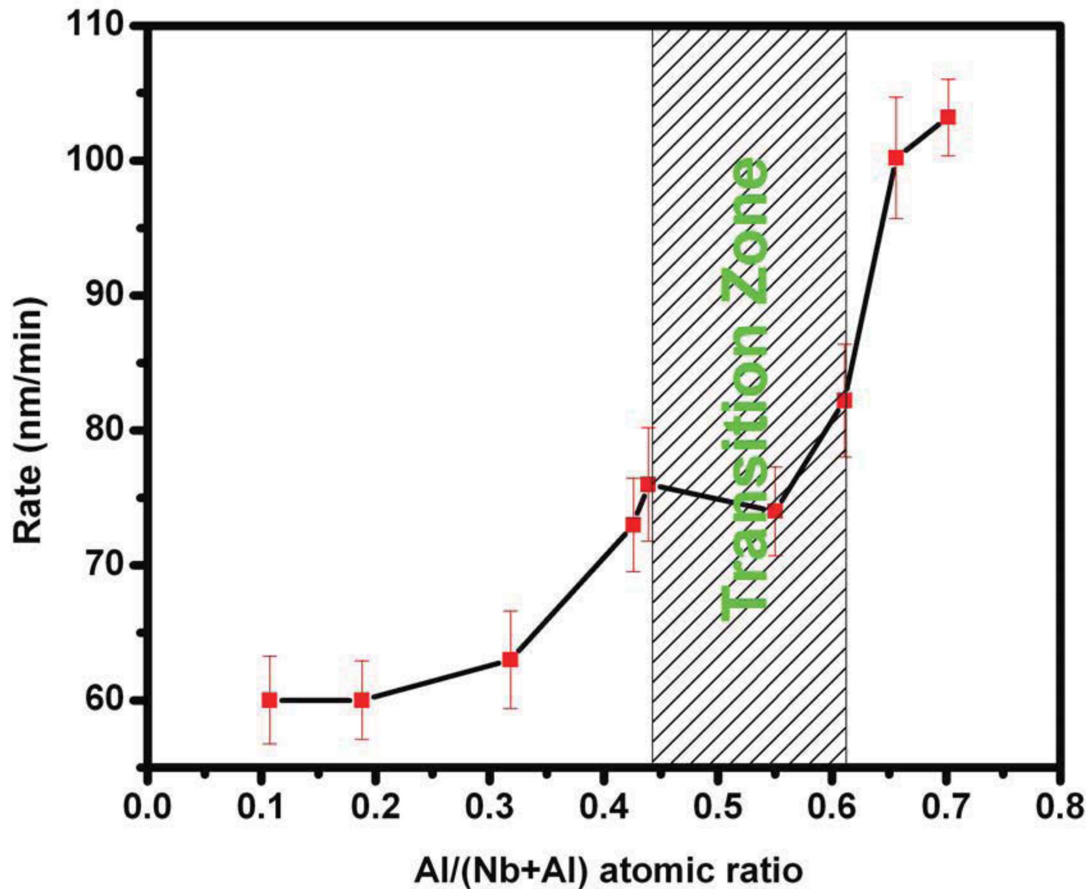

Fig. 5.17: Growth rate of $Nb_{1-x}Al_xN$ as a function of Al-content.

As shown in Fig. 5.17, initially the deposition rate increases from 60 nm/min to 76 nm/min with increasing Al ratio from x = 0.10 to 0.44. With appearance of a mixed cubic+wurtzite structure for $0.44 \leq x \leq 0.61$ the growth rate increases from 76 nm/min to 82 nm/min. Finally, the single phase wur-$Nb_{1-x}Al_xN$ increases from 82 nm/min to 103 nm/min with increasing Al content from x = 0.62 to x = 0.70, respectively. It is noteworthy, that the deposition rate is increasing with increasing hexagonal phase due to its lower density as compared to the cubic phase.

5.3.6 Mechanical properties of $Nb_{1-x}Al_xN$

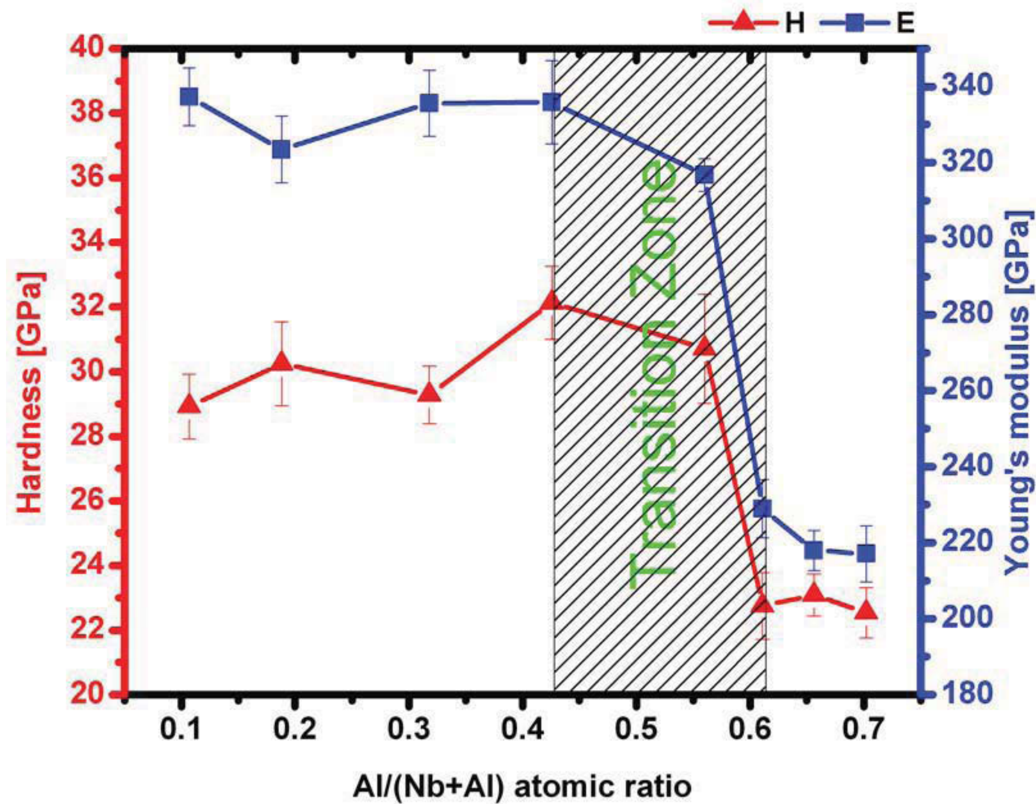

Fig. 5.18: Hardness and Young's modulus of as-deposited $Nb_{1-x}Al_xN$-coatings.

The measured hardness and Young's modulus of the $Nb_{1-x}Al_xN$ films are shown as a function of their Al/(Nb+Al) atomic ratio x in Fig. 5.18. Increasing the Al content from x = 0.11 to x = 0.44 in $Nb_{1-x}Al_xN$ films results in an increase in hardness from ~28.9 GPa to 32.1 GPa, which corresponds to the single phase cubic region fcc-$Nb_{1-x}Al_xN$, as seen in Fig. 5.18. However, further increasing the Al content causes a significant decrease in hardness due to the structural transition from the single phase region into a dual phase structure of fcc-$Nb_{1-x}Al_xN$ and wur-$Nb_{1-x}Al_xN$. A further increase of the Al content from x = 0.61 to 0.70 results in an almost constant hardness in the range of ~22-23 GPa. The variation of the Young's modulus goes along with the obtained hardness values.

5.4 $Ta_{1-x}Al_xN$-thin films

5.4.1 Processing conditions and chemical compostions of $Ta_{1-x}Al_xN$

$Ta_{1-x}Al_xN$ films were deposited onto austenitic stainless steel substrates by increasing the number of Al platelets on the Ta target race track as described in chapter 4.1.2, Fig. 4.2. Table 5.6 shows detailed information of all deposited coatings. Elemental analysis by EDX reveals that the $Ta_{1-x}Al_xN$ films are over-stoichiometric with N/metal ratios between 1.09 and 1.28, see Table 5.6. Similar to the deposition of $Nb_{1-x}Al_xN$, the Al content was increased by adding Al-platelets on the Ta-target from x = 0.11 to 0.73.

Table 5.6: Chemical composition of the deposited films and used numbers of Al platelets on the Ta-target during deposition with P_T = 0.45 Pa, P_{N2}/ P_T = 26%, T_s = 500 °C, and V_b = -50 V.

Coating	Al-platelets	Ta [at.%]	Al [at.%]	N [at.%]	N/(Al+Ta)	Al/(Ta+Al)
TaN	0	48.02	0	51.98	1.08	0
Ta(Al)N	4	50.16	< 2	49.84	1.00	0
$Ta_{0.89}Al_{0.11}N$	8	41.86	5.25	52.89	1.12	0.11
$Ta_{0.80}Al_{0.20}N$	12	34.95	8.90	56.15	1.28	0.20
$Ta_{0.75}Al_{0.25}N$	16	33.22	11.11	55.66	1.26	0.25
$Ta_{0.64}Al_{0.36}N$	20	28.31	15.62	56.08	1.28	0.36
$Ta_{0.59}Al_{0.41}N$	24	28.36	19.38	52.26	1.09	0.41
$Ta_{0.52}Al_{0.48}N$	28	24.35	22.36	53.29	1.14	0.48
$Ta_{0.45}Al_{0.55}N$	32	21.06	25.29	53.65	1.16	0.55
$Ta_{0.35}Al_{0.65}N$	36	15.40	28.90	55.70	1.26	0.65
$Ta_{0.27}Al_{0.73}N$	40	12.36	32.67	54.97	1.22	0.73

5.4.2 Colours of $Ta_{1-x}Al_xN$

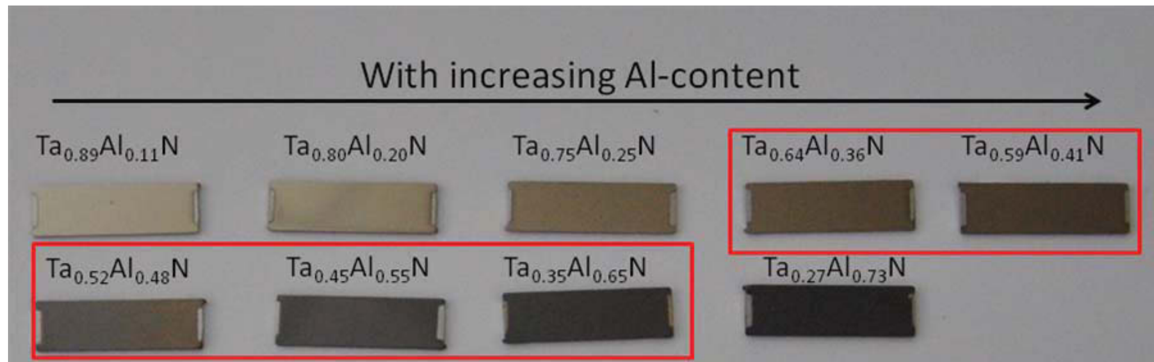

Fig. 5.19: Different colours with increasing Al-content of the $Ta_{1-x}Al_xN$ coatings.

The colours of the $Ta_{1-x}Al_xN$ coatings are changing from golden to grey to dark grey with increasing Al content, as seen in Fig. 5.19. The cubic phase region, see next chapter, indicate golden colour corresponding to chemical composition from x = 0.11 to x = 0.36. A gradually darkening grey colour occurs in the transition zone in the range from x = 0.36 to 0.65. A further incresase of Al to x = 0.65 is turning the colour to metallic grey corresponding to a singel phase hexagonal structure, see next chapter.

5.4.3 Phases of $Ta_{1-x}Al_xN$

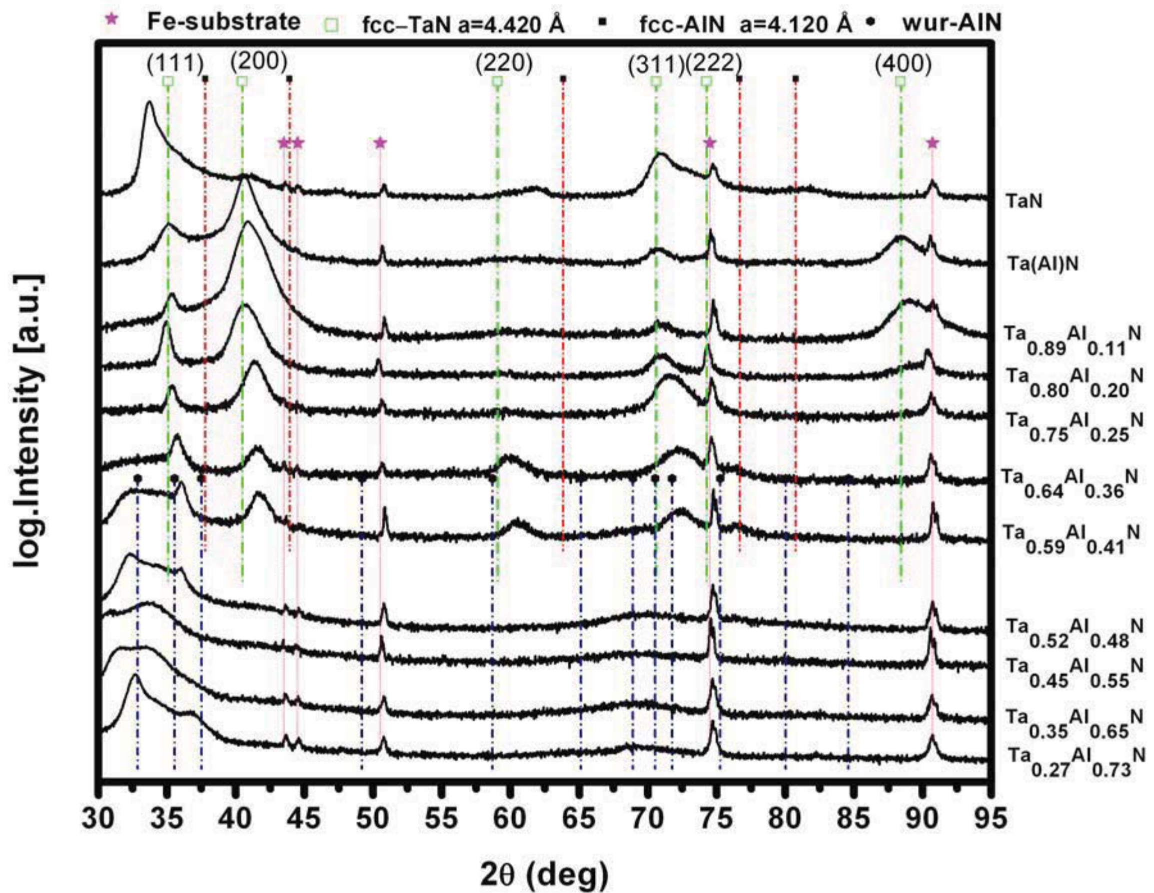

Fig. 5.20: XRD patterns of $Ta_{1-x}Al_xN$ coatings.

As shown in Fig. 5.20, the $Ta_{1-x}Al_xN$ films exhibit a single-phase cubic structure with increasing Al content from x = 0.11 to x = 0.36. The diffraction peaks shift to higher angle due to the Ta-substitution of Al atoms with smaller atomic radius in $Ta_{1-x}Al_xN$. Compared to $Nb_{1-x}Al_xN$ films, the $Ta_{1-x}Al_xN$ films present an earlier structural transition into a mixed cubic-wurtzite structure, see Fig. 5.20. Furthermore a dual phase of hexagonal-wurtzite structure is obtained by increasing the Al content on the metallic sublattice up to x = 0.48. Further increasing the Al-content promotes the hexagonal phase and for x≥0.65, the films exhibit a single phase wurtzite structure.

5.4.4 Lattice parameters of $Ta_{1-x}Al_xN$

(a)

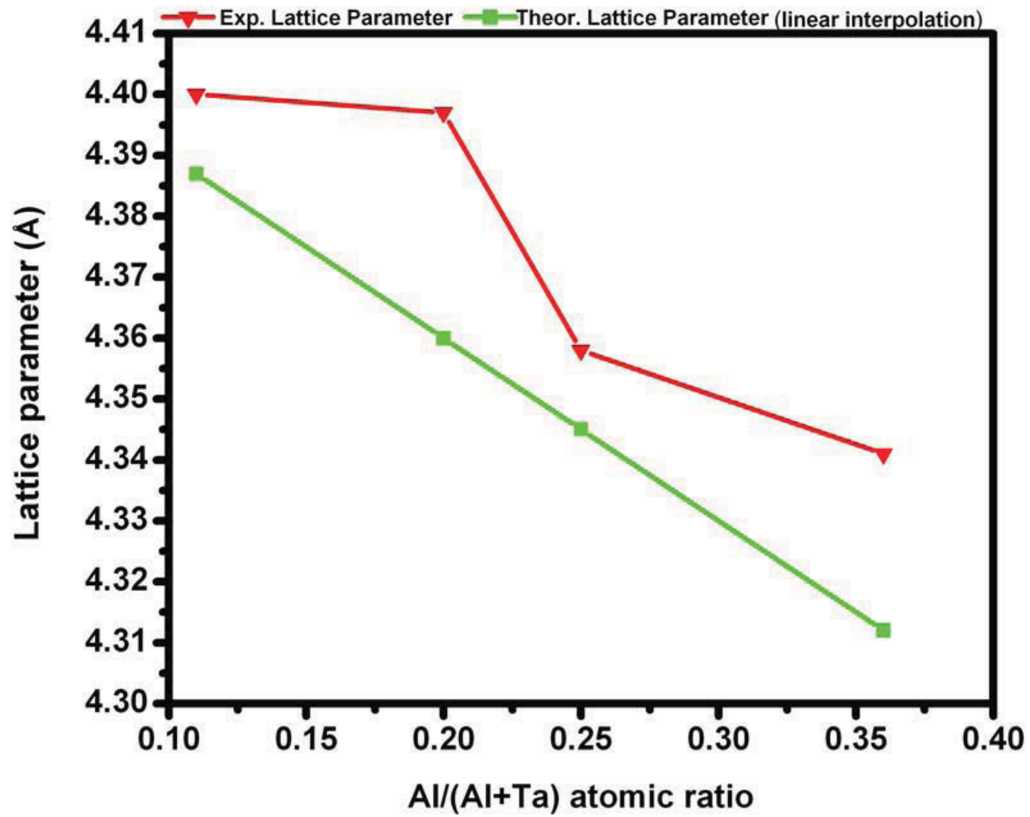

(b)

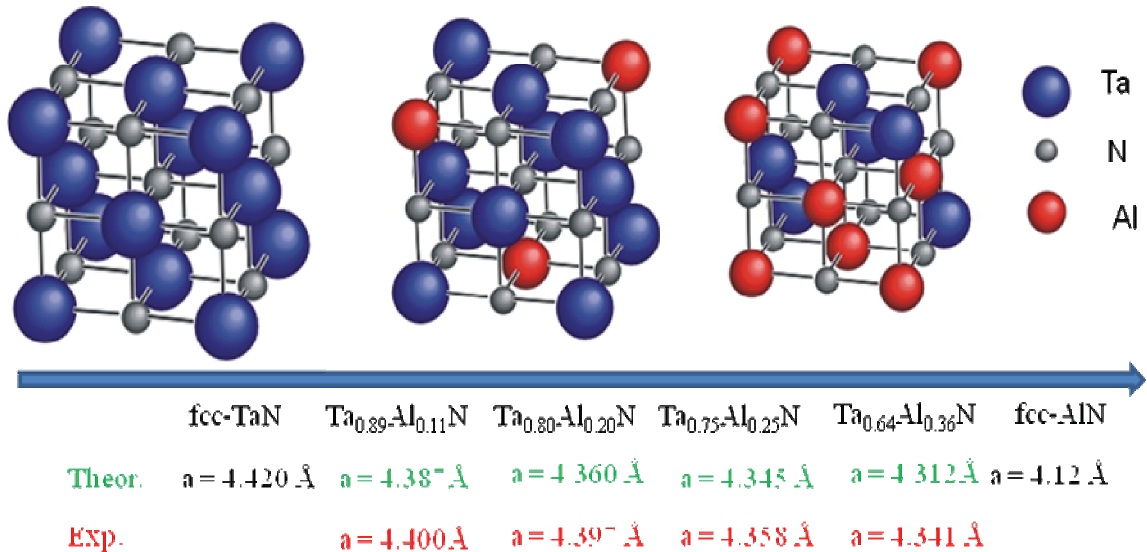

Fig. 5.21: (a) Lattice parameter of $Ta_{1-x}Al_xN$ as a function of Al-content. (b) Schematic representation of the solid-solution in a fcc-$Ta_{1-x}Al_xN$ crystal.

As shown in Fig. 5.21, the lattice parameter of the cubic $Ta_{1-x}Al_xN$ films decreases from 4.400 to 4.397 to 4.358 to 4.341 Å with increasing Al-content from x = 11 to 0.20 to 0.25 to 0.36, as determined by the Cohen-Wagner method [51]. The lattice constants of the cubic binaries a_{TaN} and a_{AlN} are 4.420 Å [52] and 4.12 Å [54] from literatur. The theoretical lattice parameter was calculated by applying Vegard's rule reaching values of 4.387, 4.360, 4.345 and 4.312 Å for Al contents x = 0.11, 0.20, 0.25 and 0.36, respectively. Using the formula (5.1), results in deviations from Vegard's rule of δ = 0.132, 0.231, 0.069, and 0.126 Å for the Al/(Ta+Al) contents of x = 0.11, 0.20, 0.25 amd 0.36.

5.4.5 Growth rate of $Ta_{1-x}Al_xN$

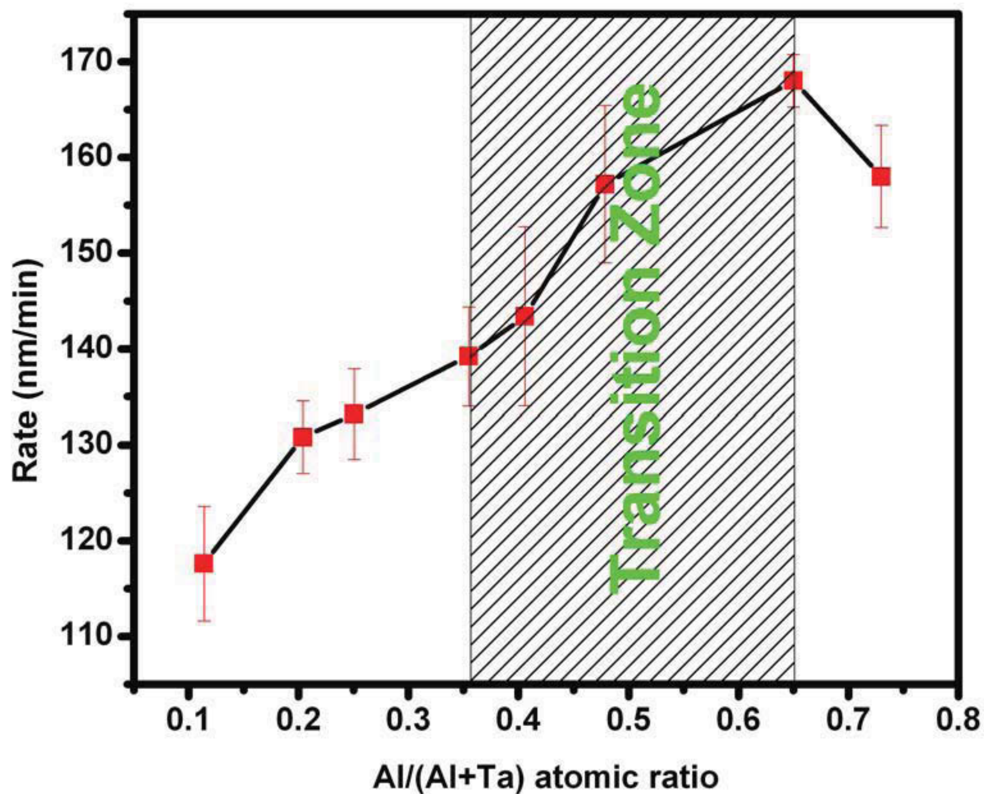

Fig. 5.22: Growth rate of $Ta_{1-x}Al_xN$ as a function of Al-content.

As shown in Fig. 5.22, the deposition rate of the Ta-Al-N films increases with increasing Al content. When compared with the deposition rate of $Nb_{1-x}Al_xN$, $Ta_{1-x}Al_xN$ films exhibit a higher growth rate at comparable Al contents. As shown in Fig. 5.22, the initial deposition

rate increases from 118 nm/min to 139 nm/min with increasing Al content x from 0.11 to 0.36. At a mixed cubic+wurtzite structure for $0.36 \leq x \leq 0.48$ a slight increased growth rate from 139 nm/min to 143 nm/min occurred. Furthermore, the unit cell volume of the wurtzite phase V_h is ~26% larger as compared to the cubic volume [29]. The growth rate increases rapidly to 168 nm/min with increasing fraction of the wurtzite phase.

5.4.6 Mechanical properties of $Ta_{1-x}Al_xN$

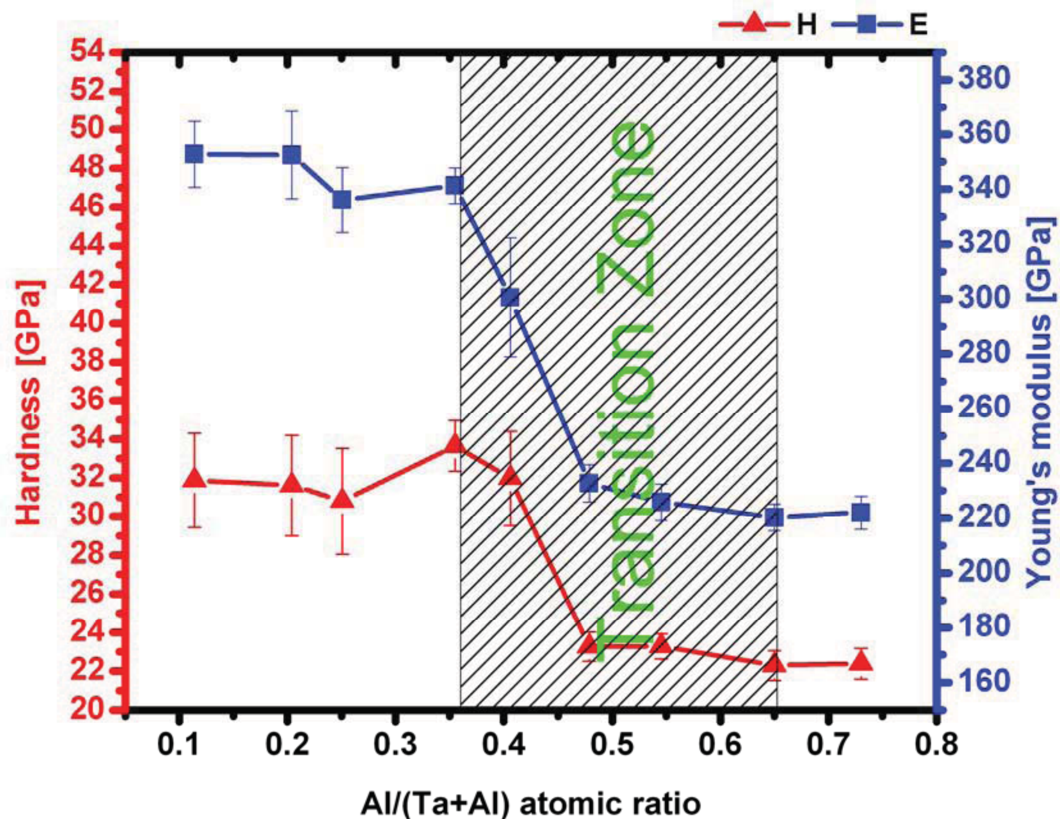

Fig. 5.23: Hardness and Young's modulus of as-deposited $Ta_{1-x}Al_xN$-coatings.

The values by nanoindentation obtained for hardness and indentation modulus of the $Ta_{1-x}Al_xN$ films are shown as a function of their Al/(Ta+Al) atomic ratio x in Fig. 5.23. Compared to $Nb_{1-x}Al_xN$, $Ta_{1-x}Al_xN$ exhibit only a small hardness increase as a function of their Al content in the single phase cubic region. Increasing the Al content x from 0.11 to 0.36 in $Ta_{1-x}Al_xN$ films results in an increase of their hardness from 31.9 GPa to 33.7 GPa, whereby all coatings show a single phase fcc-$Ta_{1-x}Al_xN$ structure, see Fig. 5.23. However, a further increase of Al causes a significant decrease in hardness due to the structural transition from

single phase fcc-$Ta_{1-x}Al_xN$ to mixed dual phases fcc-$Ta_{1-x}Al_xN$ and wur-$Ta_{1-x}Al_xN$. With increasing the Al content to x = 0.55 the hardness value is ~24 GPa, where the coatings are almost single phase hexagonal. Furthermore the Young's modulus shows a similar trend as the hardness.

6. Summary and conclusion

The aim of this thesis is to analyze the influence of Al on fcc-NbN and fcc-TaN coatings. These coatings are very attractive in terms of oxidation resistance and mechanical properties. In this work, a series of NbN_y and TaN_y coatings were deposited on Si- and austenitic stainless steel substrates with an increasing N_2 partial pressure by a reactive unbalanced magnetron sputtering technique. These studies were necessary to find the deposition parameters to grow a single-phase face centered cubic (fcc) NbN and TaN layer. Furthermore, the fcc-NbN and fcc-TaN phases are alloyed with Al to form a ternary $Nb_{1-x}Al_xN$ and $Ta_{1-x}Al_xN$ compound.

The prepared NbN_y-thin films contain ratio y of N/Nb in the range from 0.59 to 1.36 by increasing the N_2-partial pressure ratio from 16% to 100%. With increasing N_2-partial pressure during sputtering of a Nb-target the obtained coatings crystallize to form hex-Nb_2N, hex-Nb_2N+fcc-NbN, hex-NbN+fcc-NbN and finally almost single-phase fcc-NbN (measured by X-ray diffraction, XRD). The mechanical properties of these coatings are measured by nanoindentation. The hardness of the hex-NbN phase reaches ~ 38 GPa, whereas the hardness of the fcc-NbN is approximately ~28 GPa. In contrast, with increasing the N_2-partial pressure ratio from 16% to 100% cause a changed ratio y of N/Ta in the range from 0.47 to 1.61, and the TaN_y films crystallize from hex-Ta_2N, hex-Ta_2N+fcc-TaN, fcc-TaN+hex-TaN, and finally almost single phase of hex-Ta_5N_6. The single phase fcc-TaN could not be found, nevertheless the hardness value can be assumed to be ~29 GPa, as suggested by the high fcc-TaN containing dual-phase coating.

Furthermore, the fcc-NbN and fcc-TaN alloyed with Al-content increasing from x = 0.11 to 0.70 formed a ternary systems of $Nb_{1-x}Al_xN$ and $Ta_{1-x}Al_xN$. Due to incorporation of Al atoms into the crystal lattice, i.e. formation of a solid solution, higher hardness values could be obtained for the coatings. The hardness of fcc-$Nb_{1-x}Al_xN$ increases from ~28.9 to ~32.1 GPa with increasing Al-content in the range from x = 0.11 to 0.44. Then the hardness decrease from ~32.1 GPa to ~22 GPa in the range from x = 0.44 to 0.61, as the hexagonal phase is promoted and a dual phase of fcc-$Nb_{1-x}Al_xN$ and wur-$Nb_{1-x}Al_xN$ developes. A single phase wur-$Nb_{1-x}Al_xN$ exists for x>0.61 with hardness values of ~22-23 GPa. In contrast, the hardness of fcc-$Ta_{1-x}Al_xN$ increase only from ~31.9 GPa to ~33.7 GPa with increasing Al-content in the range form x = 0.11 to 0.36. The transition zone to the single-phase wurtzite

structure is in the range from x = 0.36 to 0.65 with a dual phase of fcc-$Ta_{1-x}Al_xN$ and wur-$Ta_{1-x}Al_xN$. This is connected with a hardness decrease from ~33.7 GPa to ~23 GPa. The hardness values of single phase wur-$Ta_{1-x}Al_xN$ are around ~23-24 GPa.

The NbN_y and TaN_y films present a high complexity due to the variety of crystallographic phases that can be formed. Through the incorporation of Al atoms into the crystal lattice the fcc structure is stabilised for x below 0.44 ($Nb_{1-x}Al_xN$) and 0.36 ($Ta_{1-x}Al_xN$) higher Al contents promote the formation of the wurtzite phase, higher hardness and Young's modulus values were obtained for fcc-$Nb_xAl_{1-x}N$ and fcc-$Ta_xAl_{1-x}N$.

References

[1] A. Cavaleiro, J.Th.M. De Hosson, *Nanostructured Coatings*, Springer Verlag, New York, 2006.

[2] P.H. Mayrhofer, F.D. Fischer, H.J. Böhm, C. Mitterer, J.M. Schneider, *Energetic balance and kinetics for the decomposition of supersaturated* $Ti_{1-x}Al_xN$, Acta Materialia, 55 (2007) 1441-1446.

[3] K. Kutschej, P.H. Mayrhofer, M. Kathrein, P. Polick, R. Tessadri, C. Mitterer, *Structure, mechanical and tribological properties of sputtered* $Ti_{1-x}Al_xN$ *coatings with* $0.5 \leq x \leq 0.75$, Surface and Coatings Technology, 200 (2005) 2358-2365.

[4] S.K. Kim, B.C. Cha, J.S. Yoo, *Deposition of NbN thin films by DC magnetron sputtering process*, Surface and Coatings Technology, 177-178 (2004) 434-440.

[5] M. Grosser, M. Münch, J. Brenner, M. Wilke, H. Seidel, C. Bienert, A. Roosen, U. Schmid, *Study on microstructural, chemical and properties of tantalum nitride thin films deposited by reactive direct current magnetron sputtering*, Microsystem Technologies, 16 (2010) 825-836.

[6] J.S. Brunell-Gray, P.K. Datta, *Surface Engineering Casebook*, Woodhead Publishing Ltd., Cambridge, 1996.

[7] J.R. Davis, *Surface engineering for corrosion and wear resistance,* Maney Publishing, United States of America, 2001.

[8] F.W. Bach, K. Möhwald, A. Laarmann, T. Wenz, *Modern Surface Technology*, WILEY VCH Verlag, Weinheim, 2006.

[9] M. Ohring, *Materials science of thin films*, ACADEMIC PRESS, San Diego, 2001.

[10] M. Konuma, *Film Deposition by Plasma Techniques*, Springer-Verlag, New York, London, 1992.

[11] W. Gissler, H.A. Jehn, *Advanced Techniques for surface Engineering*, Kluwer Academic Publishers, 1992.

[12] R.A. Häfer, *Oberflächen- und Dünnschicht- Technologie, Teil I: Beschichtungen von Oberflächen*, Springer Verlag, Berlin, Heidelberg, 1987.

[13] M.S. Wong, W.D. Sproul, S.L. Rohde, *Modeling magnetic fields of magnetron sputtering systems*, Surface and Coatings Technology, 49 (1991) 121-126.

[14] P.H. Mayrhofer, PhD Thesis, *Materials science aspects of nanocrystalline PVD hard coatings*, Department of Physical Metallurgy and Materials Testing, University of Leoben, Leoben, 2001.

[15] R.F. Bunshah, *Handbook of hard coatings: deposition technologies, properties and applications*, Noyes Publication, Park Ridge, New Jersey, 2001.

[16] J.E. Greene, *Handbook of Crystal Growth*, Elsevier Science Publischers, Amsterdam, 1993.

[17] H.A. Jehn, *Advanced Techniques for Surface Engineering*, edited W. Gissler, H.A. Jehn, Kluwer Academic Publischers, Dordrecht, 1992.

[18] B.A. Movchan, A.V. Demchishin, *Study of the structure and properties of thick vacuum condensates of nickel, titanium, tungsten, aluminum oxide, and zirconium dioxide*, Physics of Metals and Metallography, 28 (4) (1969) 83.

[19] J.A. Thornton, *Influence of apparatus geometry and deposition conditions on the structure and topography of thick sputtered coating*, Journal of Vacuum Science and Technology, 11 (4) (1974) 666-670.

[20] J.A. Thornton, *Influence of substrate temperature and deposition rate on structure of thick sputtered Cu coatings*, Journal of Vacuum Science and Technology, 12 (4) (1975) 830-835.

[21] R. Messier, A.P. Giri, R.A. Roy, *Revised structure zone model for thin film physical structure*, Journal of Vacuum Science and Technology, A 2 (1984) 500.

[22] P.B. Barna, M. Adamik, *Protective Coatings and Thin Films,* edited Y. Pauleau, P.B. Barna, Kluwer Academic Publishers, Dordrecht, 1996.

[23] J.A. Thornton, *High rate thick film growth*, Annual Review of Materials. Science, 7 (1977) 239.

[24] http://elib.uni-stuttgart.de/opus/volltexte/2005/2467/pdf/Teil2.pdf

[25] http://www.springermaterials.com/docs/pdf/10522884_2118.html

[26] http://www.springermaterials.com/docs/pdf/10522884_2136.html

[27] S. PalDey. S.C. Deevi, *A Structural Materials Propperties Microstructure and Processing*, Materials Science and Engineering, 342 (2003) 58.

[28] M. Moser, PhD Thesis, *Structural evolution of protective coatings for γ-TiAl based alloys*, Department of Physical Metallurgy and Materials Testing, University of Leoben, Leoben, 2008.

[29] R. Rachbauer, Diploma Thesis, *Comparative microstructural investigations of Ti-Al-N thin films alloyed with Y or Nb*, Department of Physical Metallurgy and Materials Testing, University of Leoben, Leoben, 2008.

[30] R. Franz, M. Lechthaler, C. Polyer, C. Mitterer, *Structure, Mechanical properties and oxidation behaviour of arc-evaporated NbAlN hard coatings*, Surface and Coatings Technology, 204 (2010) 2447-2453.

[31] M. Zhou, Y. Makino, M. Nose, K. Nogi, *Phase transition and properties of Ti-Al-N thin films prepared by r.f.-plasma assisted magnetron sputtering*, Thin Solid Films, 339 (1999) 203-208.

[32] User Manual A400 VL, Leybold AG.

[33] Operational Manual ACG-6B, ENI Company Ltd.

[34] User Guide Leybold Vacuum, Leybold, AG.

[35] User Guide Tylan General R 7030/7031, Tylan General GmbH.

[36] User Manual Duo 20, Pfeiffer Vacuum GmbH, 2002.

[37] W.H. Bragg, W.L. Bragg, *Proceedings of the Royal Society of London*. Series A, Containing Papers of a Mathematical and Physical Character, 88/605 (1913) 428.

[38] H. Willmann, PhD Thesis, *Al-Cr-N thin film design for high temperature applications*, Department of Physical Metallurgy and Materials Testing, University of Leoben, Leoben, 2007.

[39] B.E. Warren, *X-Ray Diffraction*, Dover Publications, New York, 1990.

[40] D. Brandon, W.D. Kaplan, *Microstructural Characterization of Materials*, John Wiley and Sons Ltd, Israel, 2008.

[41] K. Nitzsche, *Schichtmesstechnik*, Vogel, Würzburg, 1997.

[42] A.C. Fischer-Cripps, *Nanoindentation*, Springer Science and Business Media LLC, New York, 2006.

[43] A. Cavaleiro, J.Th.M. De Hosson, *Nanostructured Coatings*, Springer, New York, 2006.

[44] R. Saha, W.D. Nix, *Effects of the substrate on the determination of the thin film mechanical properties by nanoindentation*, Acta Materialia, 50 (2002) 23-38.

[45] IBIS, Fischer-Cripps Laboratory.

[46] G.A. Fontalvo, V. Terziyska, C. Mitterer, *High-temperature tribological behaviour of sputtered* NbN_x *thin films*, Surface and Coatings Technology, 202 (2007) 1017-1022.

[47] R. Sanjinés, M. Benkahoul, C.S. Sandu, P.E. Schmid, F. Lévy, *Electronic states and physical properties of hexagonal β-Nb_2N and δ´-NbN nitrides*, Thin soild Films, 494 (2006) 190-195.

[48] C.S. Shin, Y.W. Kim, D. Gall, J.E. Greene, I. Petrov, *Phase composition and micro-structure of polycrystalline and epitaxial TaN_x Layers grown on oxidized Si (001) and MgO (001) by reactive magnetron sputter deposition*, Thin soild Films, 402 (2002) 172-182.

[49] G.R. Lee, J.J. Lee, C.S. Shin, I. Petrov, J.E. Greene, *Self-organized lamellar tantalum-nitride by UHV unbalance-magnetron sputtering*, Thin Solid Films, 475 (2005) 45-48.

[50] T.L. Selinder, D.J. Miller, K.E. Gray, *Phase formation and microstructure of $Nb_{1-x}Al_x$-N alloy films grown on MgO (100) by reactive sputtering a new ternary phase*, Vacuum, 46 (1995) 1401-1406.

[51] C.N.J. Wagner, *Local Atomic Arrangements Stuied by X-ray diffraction (Gordon and Breach)*, Now York, Vol. 7, 1966.

[52] R. Rachbauer, D. Holec, P.H. Mayrhofer, *Phase stability and decomposition of Ti-Al-Ta-N thin films*, APPLIED PHYSICS LETTERS, 97 (2010) 151901

[53] L. Vegrad, *Die konstitution der Mischkristalle und die Raumfüllung der Atome*, Physikalisches Insititut, 1921.

[54] JCPDS Card Nos, 00-25-1495.

[55] JCPDS Card Nos, 01-089-5129, 01-089-5131, 01-089-4756, 01-071-0162, 01-074-5125, 01-074-0607.

[56] JPDSC Card Nos, 01-089-4764, 03-065-9404, 01-071-0253, 00-049-1284, 01-075-0628.